



Assessment of Self-Healing Epoxy-Based Coatings Containing Microcapsules Applied on Hot Dipped Galvanized Steel

*Evangelia K. Karaxi, Ioannis A. Kartsonakis and Costas A. Charitidis**

Research Unit of Advanced, Composite, Nanomaterials and Nanotechnology, School of Chemical Engineering, National Technical University of Athens, Athens, Greece

This study focuses on the design, development, and validation of two coating systems for corrosion protection of hot dip galvanized steel substrates. The coatings consist of epoxy-based resin reinforced with core-shell microcapsules, either cerium oxide or cuprous oxide core and a polymeric shell doped with cerium ions. The effect of the modification of the epoxy resin with a liquid rubber polymer has also been studied. Corrosion studies via electrochemical impedance spectroscopy (EIS) revealed that the coatings have enhanced barrier properties. Moreover, EIS studies on coatings with artificial scribes, demonstrated an autonomous response to damage and a self-healing effect. Heat-induced material re-flow has also been observed after exposure to temperature higher than the T_g of the system, which offered an additional self-healing mechanism, partially inhibiting the underlying corrosion processes when the liquid rubber is present in the system.

Keywords: self-healing (self-repairing), core/shell microcapsules, corrosion protective coatings, hot dip galvanized steel, EIS (electrochemical impedance spectroscopy)

OPEN ACCESS

Edited by:

Flavio Defforian,
University of Trento, Italy

Reviewed by:

Rita Bacelar Figueira,
University of Minho, Portugal
Fatima Montemor,
Instituto Superior Técnico, Portugal

*Correspondence:

Costas A. Charitidis
charitidis@chemeng.ntua.gr

Specialty section:

This article was submitted to
Environmental Materials,
a section of the journal
Frontiers in Materials

Received: 17 June 2019

Accepted: 28 August 2019

Published: 11 September 2019

Citation:

Karaxi EK, Kartsonakis IA and Charitidis CA (2019) Assessment of Self-Healing Epoxy-Based Coatings Containing Microcapsules Applied on Hot Dipped Galvanized Steel. *Front. Mater.* 6:222. doi: 10.3389/fmats.2019.00222

INTRODUCTION

Corrosion phenomena on metallic structures result eventually in the degradation of the metal and the deterioration of its properties. Failure of a metallic operating structure compromises the safety, which is a critical consideration during an equipment design. The degradation of engineering structures such as bridges, automobiles, airplanes, and ships due to their exposure in corrosive environments may contribute to life-threatening situations. Moreover, direct and indirect economic losses are linked to corrosion phenomena such as maintenance or replacement costs, expenses related to industry temporary shutdown, efficiency, and product losses. According to the literature, about 25–30% of this total could be avoided if currently available corrosion technology was effectively applied (Uhlig, 2008).

Eventually, all coatings develop defects which are responsible for the direct access of corrosive agents to the metallic substrate. Chromate-based conversion coatings are the most popular all over the world as a pretreatment strategy for a variety of substrates because they offer re-passivation of the corroded area, so hexavalent chromium remains the most effective corrosion preventive compound to date (Gharbi et al., 2018) which is still used in advanced applications (e.g., aerospace). Unfortunately, chromates are long known as environmentally unfriendly and life-threatening compounds due to their leachability and superior oxidation properties, which render

them responsible for DNA damage and cancer (Levina et al., 2006; OSHA3373-10, 2009). The most widely used alternative corrosion prevention measure, is the application of organic coatings with less toxic organic and inorganic additives that are able to provide a dense barrier against corrosive species (Kartsonakis et al., 2013; Figueira et al., 2014; Upadhyay and Battocchi, 2016; Lyon et al., 2017). The recent research activity in the corrosion protection field is focused on the development of new coatings incorporating self-healing characteristics being able to extend the service-life of the coating. The main desired achievement in self-healing coatings is the restoration of their protective performance with minimal or no external intervention (Zhang et al., 2018). According to the same recent review article, self-healing coatings can be categorized in two broad categories, autonomous and non-autonomous coating systems, depending on the mechanism of the onset of healing action (triggered or not). The most common self-healing mechanisms reported in literature are based on (i) polymerizable healants (Zhu et al., 2015; Balaskas et al., 2017), (ii) encapsulated corrosion inhibitors, (iii) reversible bonds, and (iv) reversible chain conformation (Abdolah Zadeh et al., 2016; Samiee et al., 2019). Thus, protective coatings can be characterized by damage-responsive functionalities which result in defect healing/sealing action and/or active corrosion protection by inhibiting corrosion reactions (Kakaroglou et al., 2016; Snihirova et al., 2016; Ulaeto et al., 2017).

Thus, along with the barrier properties, a corrosion protection mechanism responsive to damage has become a promising strategy in order to deliver a coating system with long-term corrosion protection effect. A more sophisticated system dictates, ideally, the occurrence of multiple self-healing events in an autonomous way based on the intrinsic characteristics of the coating system (Yin et al., 2015; Das et al., 2016). The incorporation of actively responsive sub-micron materials in a corrosion protective system can be considered as a favorable pathway to ensure the recovery of its main function, namely, hindering of the corrosion activity.

However, thermoset epoxy-based networks, which are one of the most widely used in coating applications, have many undesirable features, i.e., they have poor resistance to impact and crack growth, which limits their application to certain technological areas. The fracture energy of an epoxy resin is two and three orders of magnitude smaller than thermoplastic polymers and metals. This suggests the need to strengthen these systems in order to expand their applications (Comstock et al., 1989; Figueira et al., 2014).

Hence, the modification of epoxy resins to enhance their brittleness has received considerable research interest. Many research efforts have been reported since 1970, where the first resin modifications with secondary elastomeric phases was initiated by McGarry (1970) and then extensive research has been focused on the investigation and understanding of the toughening mechanism of rubber-toughened epoxies (Yee and Pearson, 1986; Vázquez et al., 1987; Garg and Mai, 1988; Yamanaka et al., 1989; Verchere et al., 1990; Iijima et al., 1991; Williams et al., 1997; Ratna, 2001; Ratna and Banthia,

2004; Bagheri et al., 2009; Unnikrishnan and Thachil, 2012; Parameswaranpillai et al., 2017).

In addition, another limitation arises from the direct addition of inorganic capsules in self-healing epoxy coatings which is their limited compatibility of the inert inorganic surface with the organic coating. The coating's protective performance and adhesion properties are severely affected due to particle agglomeration and defect formation at the interface of these incompatible materials, which are also a function of the concentration and size of the containers and the coating's thickness, as reported by recent research and review articles (Kartsonakis et al., 2010; Borisova et al., 2013; Zhang et al., 2018). A way through these phenomena is the surface modification and decoration of the inorganic surfaces which gives endless options and possibilities to manufacture an engineered microstructure with the desired functional characteristics and limit compatibility issues in epoxy coatings (Skorb et al., 2009; Kainourgiou et al., 2017; Kongparakul et al., 2017; Li et al., 2017).

The motivation for this work is to develop a new multifunctional smart coating system, with self-healing characteristics which contribute to its protective anticorrosion properties. Thus, the main aim of this study is to evaluate the self-healing responsiveness and corresponding barrier properties of two developed advanced coating systems. Both samples consist of a hybrid organic-inorganic epoxy coating toughened by the addition of an organically modified silicate. Core-shell modified cerium oxide (CeO_2) and cuprous oxide (Cu_2O) microcapsules were incorporated into the epoxy-based matrices. In addition, in one of the studied systems, the incorporation of a liquid rubber modifier in free form was selected to investigate its influence on the electrochemical response of the obtained coating. The hybrid organic-inorganic coatings were applied onto hot dip galvanized (HDG) steel panels.

The core-shell microcapsules were characterized with respect to their morphology and chemical composition through transmission electron microscopy (TEM), Fourier transform infrared spectroscopy (FT-IR), gel permeation chromatography (GPC), X-ray diffraction (XRD), and thermogravimetric analysis (TGA). The protective and self-healing ability of intact and scribed coatings as well as their responsiveness and their ability to restore their anticorrosion properties after thermal treatment were evaluated through electrochemical impedance spectroscopy (EIS) while immersed in selected corrosive electrolytes.

MATERIALS AND METHODS

Acetonitrile (Acros Organics), toluene (Acros Organics), acetone (Acros Organics), absolute ethanol (Acros Organics), methanol (MeOH, Acros Organics), absolute ethanol (Sigma Aldrich), N,N-dimethylformamide (DMF, Sigma Aldrich), copper acetate (Sigma Aldrich), hydrazine hydrate (N_2H_4 , 50–60%, Sigma Aldrich), cerium acetyl acetonate [$\text{Ce}(\text{acac})_3$, Sigma Aldrich], potassium peroxodisulfate (KPS, Sigma Aldrich), α -bromoisobutyryl bromide (BIBB, Sigma Aldrich), (3-aminopropyl)triethoxy silane (APTES, Sigma Aldrich), triethylamine (Sigma Aldrich), copper (II) bromide [$\text{Cu}(\text{II})\text{Br}$,

Sigma Aldrich], cerium nitrate [$\text{Ce}(\text{NO}_3)_3$, Sigma Aldrich], ammonium cerium(IV) nitrate [$\text{Ce}(\text{NH}_4)_2(\text{NO}_3)_6$, Sigma Aldrich], trifluoroacetic acid (CF_3COOH , Merck, >99%), dichloromethane (Sigma Aldrich, 99.8%), 2,2'-Bipyridyl (bpy, Sigma Aldrich), diethylenetriamine (Sigma Aldrich), ascorbic acid (Sigma Aldrich), epoxy resin based on phenol 4,4'-(1-methylethylidene) bis- (Ciba-Geigy), sodium hydroxide (Sigma Aldrich), and sodium chloride (Sigma Aldrich) were used as received. The monomers methacrylic acid (MAA) and n-butyl acrylate (nBA) and tert-butyl acrylate (tBA) were double distilled under reduced pressure prior to use.

Synthesis of Cu_2O and CeO_2 Cores

The synthesis of Cu_2O cores was performed by a simple one-pot wet chemical route using copper acetate as the precursor and hydrazine as the reducing agent. The experiment was conducted at room temperature by adding hydrazine hydrate (0.03 mol) in a copper acetate solution (0.042 M). The reaction was left to proceed under vigorous stirring for 10 min, while the solution's color changed from blue to green and finally to bright orange. The products were left to precipitate, the supernatant solution was discarded and the sediments were repeatedly washed through multiple centrifugations. The Cu_2O cores were left to dry in a vacuum desiccator.

For the production of CeO_2 cores a two-step process was followed as reported elsewhere (Kartsonakis et al., 2008, 2010). Briefly, negatively charged polymethacrylic acid (PMAA) nanospheres were synthesized through radical polymerization in acetonitrile using KPS as initiator and then utilized as templates for the formation of an inorganic surface layer composed of cerianite (CeO_2) using $\text{Ce}(\text{acac})_3$ as precursor ($\text{PMAA}@\text{CeO}_2$). Hollow CeO_2 cores were formed through the dispersion of the $\text{PMAA}@\text{CeO}_2$ composites in EtOH/ H_2O mixture (2:1) which resulted in the controlled and selective dissolution of PMAA cores. The final inorganic hollow cores were isolated through multiple centrifugations and were washed with water and ethanol.

Synthesis of Core-Shell Microcapsules

Inorganic-organic core-shell microcapsules were synthesized through surface-initiated activators regenerated by electron transfer atom transfer radical polymerization (ARGET-ATRP) process. The inorganic core materials, CeO_2 or Cu_2O , were selected due to their inherent corrosion protective and antifouling characteristics, respectively. A diblock copolymer, poly(n-butyl acrylate-b-acrylic acid) [$\text{P}(\text{BA}-b\text{-AA})$], was synthesized on the surface of cerium oxide, $\text{CeO}_2@\text{P}(\text{BA}-b\text{-AA})$, or cuprous oxide microcapsules, $\text{Cu}_2\text{O}@\text{P}(\text{BA}-b\text{-AA})$. The addition of a second PAA-based polymer block was decided in order to obtain a carboxyl-terminated block copolymer and enhance the reaction between carboxyl and oxirane groups of the epoxy matrix.

The synthesis of the diblock copolymer onto the surface of either CeO_2 or Cu_2O was performed according to the following procedure (schematic representation in **Supplementary Figure S1**): firstly, an α -bromoester initiator was tethered on the inorganic cores' surface by self-assembly

of APTES followed by amidization with BIBB. The APTES-functionalization ensures the covalent bonding of the initiator molecules with the inorganic surface. Then, surface initiated ARGET ATRP was carried out from the above-mentioned initiator-modified particles.

Either CeO_2 or Cu_2O cores were dispersed in absolute ethanol using ultra sonication in a three-neck flask equipped with a condenser and a magnetic stirrer. After heating to 70°C , APTES was added under N_2 atmosphere and the dispersion was left for 24 h under stirring. The APTES-modified inorganic cores were centrifuged, washed with ethanol and redispersed in DMF. Then BIBB was added drop-wise in the flask using triethylamine as the catalyst and left in an ice bath for 1 h under stirring in N_2 atmosphere and then at room temperature for 24 h. The macroinitiators (initiator-functionalized inorganic particles) were isolated and rinsed through centrifugation. A septum-sealed Schenk flask was used during surface initiated ARGET-ATRP. For each experiment, CeO_2 or Cu_2O cores were dispersed in toluene followed by the complete dissolution of the $\text{Cu}(\text{II})\text{Br}/\text{bpy}$ complex and the addition of the deoxygenated monomer. The nBA was used as monomer and ascorbic acid served as reducing agent for initiating the polymerization process. Then, t-BA was added to the above mixture resulting in a diblock polymer shell comprising of PnBA and PtBA. The AA block resulted from an acidolysis reaction, as reported elsewhere (Colombani et al., 2007). Detailed experimental conditions for the aforementioned synthetic procedure are given in **Table 1**. The final inorganic-organic core-shell microcapsules, $\text{CeO}_2@\text{P}(\text{BA}-b\text{-AA})$ or $\text{Cu}_2\text{O}@\text{P}(\text{BA}-b\text{-AA})$, were isolated and purified through multiple centrifugations and washings with MeOH and remained in dispersed state for further modification. The cerium-doped microcapsules were then developed by adding dropwise a 0.5% w/v cerium ammonium nitrate solution (in MeOH) to the above dispersion. The final composites were isolated again by centrifugation. Additionally, ARGET-ATRP was performed in order poly(n-butyl acrylate; PBA) to be synthesized using KPS (0.5 g), nBA (10.0 ml), and toluene (50.0 ml) as solvent at 60°C for 12 h.

Coating Synthesis and Application

The HDG steel substrates pre-treatment prior to coating application included degreasing and cleaning using acetone

TABLE 1 | The conditions used in the preparation of core/ shell microcapsules.

Material	Quantity
CeO_2 or Cu_2O cores	1.0 (g)
(3-aminopropyl)triethoxy silane	1.0 (ml)
Absolute ethanol	20.0 (ml)
N,N-dimethylformamide	20.0 (ml)
Triethylamine	1.0 (ml)
α -bromoisobutryl bromide	2.0 (ml)
Toluene	20.0 (ml)
Copper (II) bromide	0.1 (g)
2,2'-Bipyridyl	1.0 (g)
N-butyl acrylate	10.0 (ml)
Ascorbic acid	1.0 (g)

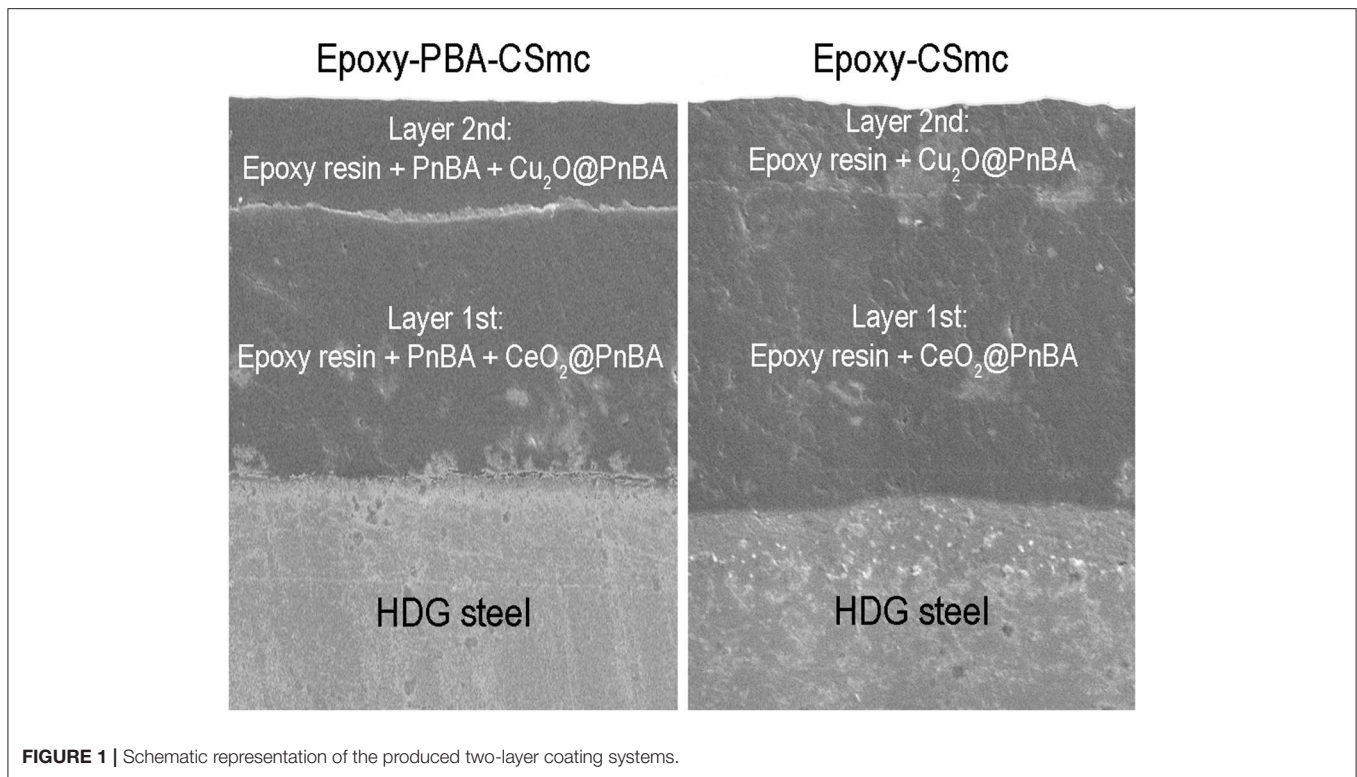


FIGURE 1 | Schematic representation of the produced two-layer coating systems.

TABLE 2 | The conditions used in the preparation of the epoxy solution.

Material	Quantity (wt.%)
(3-aminopropyl)triethoxy silane	2.0
2,2-Bis[4-(glycidyl oxy)phenyl]propane	25.0
Diethylenetriamine	2.0
PnBA	5.0
Absolute ethanol	34.0
Acetone	30.0
CeO ₂ @P(BA-b-AA) or Cu ₂ O@P(BA-b-AA) core-shell microcapsules	2.0

and NaOH solution at pH 11 for 5 min at 50°C, thoroughly washing with distilled water and their storage in a vacuum designator. Two coating systems were prepared; named *Epoxy-PBA-CSmc* and *Epoxy-CSmc* (Figure 1). The matrix of each of the two-layered coating system was based on the combination of a cross-linked epoxy polymer with organically modified silicates as described in detail in our previous work (Kartsonakis et al., 2012). The conditions used in the preparation of the epoxy solution are tabulated in Table 2. The synthesized core-shell microcapsules were incorporated as reinforcing additives in both epoxy-based hybrid coatings in a concentration of 4 wt.% and were applied with a baker film applicator onto the metallic substrates. The liquid rubber (PBA) was mixed with the epoxy-based solution prior to deposition for the preparation of the second coating system (*Epoxy-PBA-CSmc*). Finally, the as-prepared coated substrates (in triplicates for each system) were

left in a furnace at 90°C for 4 days and deposited in a vacuum designator until use.

Characterization Methods

Transmission electron microscope (TEM; JEM2000 FX, 200 KV, resolution 0.28 nm) and Fourier Transform Infrared Spectroscopy (FT-IR) were utilized for the chemical composition determination of the hybrid composites through Attenuated Total Reflectance (ATR) method with Agilent Cary 630 spectrometer.

The thermal degradation of the synthesized microcapsule materials was analyzed via thermogravimetric analysis (TGA) using a thermal analyzer apparatus (STA 449 F5 Jupiter). The samples were measured under constant nitrogen flow (50 ml/min) plus nitrogen flow as protective gas (20 ml/min) from 25 to 1,000°C at a heating rate of 10°C/min. Prior to the non-isothermal experiments the instrument was calibrated both for temperature and sensitivity. The exported data were manipulated through Proteus 6.1 Software. The polymer content was determined from the total of weight loss the microcapsules. The total organic content was then used to calculate the grafting density (σ_{TGA}) based on the core diameter established by TEM, utilizing the Equation (1) (Benoit et al., 2012):

$$\sigma_{TGA} = \frac{\frac{wt\% \text{ shell}}{wt\% \text{ core}} \times \rho_{core} \times \frac{4}{3}\pi r_{core}^3 \times N_A}{MW \times 4\pi r_{core}^2} \quad (1)$$

where the weight percentages of the shell and core materials were obtained by TGA for the temperature range 300–500°C.

The crystal structure was identified by powder X-ray diffraction (XRD) using X Bruker D8 Advance Twin Twin,

employing Cu-K α radiation ($\lambda = 1.5418 \text{ \AA}$). The thickness of the final coating system was measured with a coating thickness test instrument through the magnetic induction method (ACUTECH LTD, DUALSCOPE MP0R) and through SEM at the coatings' cross-section. In addition, Differential Scanning Calorimetry (DSC) testing was conducted on selected coating sample using Perkin Elmer Pyris 6 DSC apparatus calibrated with indium for temperature and heat capacity. Measurements were carried out in high purity nitrogen atmosphere on samples of $\sim 8 \text{ mg}$ in mass closed in standard aluminum Perkin Elmer pans. Measurement was performed on fresh sample that was heated from 20°C up to 250°C with a heating rate of $20^\circ\text{C}/\text{min}$, stayed there isothermally for 2 min, cooled down to -110°C at $30^\circ\text{C}/\text{min}$ and, finally, heated from -110°C to 350°C at $5^\circ\text{C}/\text{min}$.

The microstructure, thickness and qualitative elemental analysis of the coatings were studied by Scanning Electron Microscopy (SEM) coupled with Energy Dispersive X-Ray Spectroscopy (EDS) using a PHILIPS Quanta Inspect (FEI Company) microscope with 149 W (tungsten) filament 25 KV equipped with EDAX GENESIS (AMETEX PROCESS & 150 ANALYTICAL INSTRUMENTS). Electrochemical Impedance Spectroscopy (EIS) measurements were conducted to assess the anti-corrosive properties of coatings and to verify its corrosion mechanism. A potentiostat/galvanostat connected to a Frequency Response Analyzer (VersaStat 3/FRA, PAR AMETEK) was used with an electrochemical cell of three electrodes (K0235 Flat Cell Kit, AMETEK), consisting of a working electrode ($\sim 1 \text{ cm}^2$ exposed sample surface), a saturated silver/silver chloride electrode [Ag/AgCl, KCl (sat)] as a reference electrode and a platinum mesh electrode as the counting electrode for the measurements. The measurement frequency ranged from 100 kHz to 0.01 Hz and the sinusoidal perturbation applied was 10 mV. The spectra were analyzed through ZView[®] software (Scribner Associates) using the appropriate equivalent electrochemical circuit each time. The study of the anti-corrosion properties of the intact coating systems on galvanized steel samples included exposure to corrosive artificial ocean water prepared in accordance with ASTM D1141-98. The chemical composition of the solution is shown in **Supplementary Table T1**. As stated in the standard, the chlorinity is 19.38 and the pH of the solution (after correction with 0.1N NaOH) is 8.2. Thus, all the measurements were conducted in triplicate in a pH range from 8.2 to 9.

A second set of EIS measurements was performed on artificially scribed coated samples exposed to 5 mM NaCl solution in order to understand the mechanism of corrosion and its inhibition. For the in-depth study of the coatings and the investigation of their potential use as self-healing coating systems, artificial scribes of 1–2 mm length were created so that the metal substrate remains exposed to the electrolyte. This was confirmed for each sample by SEM analysis and the corresponding line elemental EDS analysis of the HDG metal substrate elements, Fe and Zn (**Supplementary Figure S2**). The exposed area of 1 cm^2 was carefully selected in a way that the scribe is located in its center. The interpretation of the EIS results was performed by numerical fitting using equivalent electric circuit models (Zheludkevich et al., 2005; Kartsonakis et al., 2016). Constant

phase elements (CPE) were used to account for the electrode heterogeneity. Generally, as reported in literature the CPE is related with a distribution of the capacitance over a surface or its changes with frequency which are associated with electrode heterogeneity (Montemor et al., 2008; Plawecka et al., 2014). Therefore, in the equivalent circuits worked with in our study, CPE were used instead of pure capacitors. This modification is obligatory when the phase shift of a capacitor is different from -90° (Hsu and Mansfeld, 2001). The impedance of an R-CPE parallel association is given by:

$$Z_{R-CPE} = \frac{R}{1 + RY_0(j\omega)^n} \quad (2)$$

where Y_0 is the admittance of the CPE and n is the CPE exponent. The n equals to 1 when it corresponds to a capacitor, it takes the values $0.5 < n < 1$ when a non-ideal capacitor behavior takes place, n equals to 0.5 when the CPE describes a diffusion process and represents a Warburg impedance, and finally, n equals to 0 when it represents a resistor (Orazem and Tribollet, 2008; Zhu et al., 2016).

Using the Cole-Cole approach together with CPE (Cole and Cole, 1942; Barsoukov and Macdonald, 2018), the capacitance can be calculated by numerical fitting through the Equation (3):

$$C = \sqrt[n]{\frac{RY_0}{R^n}} \quad (3)$$

In addition, the investigation of a thermally-induced self-healing mechanism was conducted. Both the two-layer coating systems were subjected to the formation of a defect in a way that the underlying metal is exposed. Microscopic observation was then performed through SEM along with elemental mapping. The anticorrosion protection performance of each scribed coating was evaluated through EIS immediately after SEM analysis through the exposure to 5 mM NaCl solution. The samples were dried and were thermally treated at 90°C for 30 min and their corrosion behavior via EIS was again measured once. The low frequency impedance values were compared before and after heat treatment in order to evaluate the recovery of the barrier properties, the main function of the coatings studied.

RESULTS AND DISCUSSION

Figures 2, 3 depict the TEM images of the $\text{CeO}_2@P(\text{BA}-b\text{-AA})$ and $\text{Cu}_2\text{O}@P(\text{BA}-b\text{-AA})$ core-shell microcapsules, respectively. Regarding **Figure 2a**, it may be remarked that the $\text{CeO}_2@P(\text{BA}-b\text{-AA})$ sample consists of spherical hybrid microcapsules with a core-shell configuration with average diameter size $600 \pm 150 \text{ nm}$. The shell is amorphous (dark contrast ring) and its average thickness is $30 \pm 10 \text{ nm}$, while the core is nanocrystalline (lighter contrast) comprising of randomly oriented nanocrystals with a diameter range of 2–3 nm (**Figure 2b**), as illustrated by high-resolution TEM (HRTEM). According to HRTEM image that depicts the atomic structure of the core nanocrystals, the 3.12 Å interplanar spacing of the {111} crystal planes of CeO_2 is clearly resolved. The crystal structure of the nanocrystalline core was

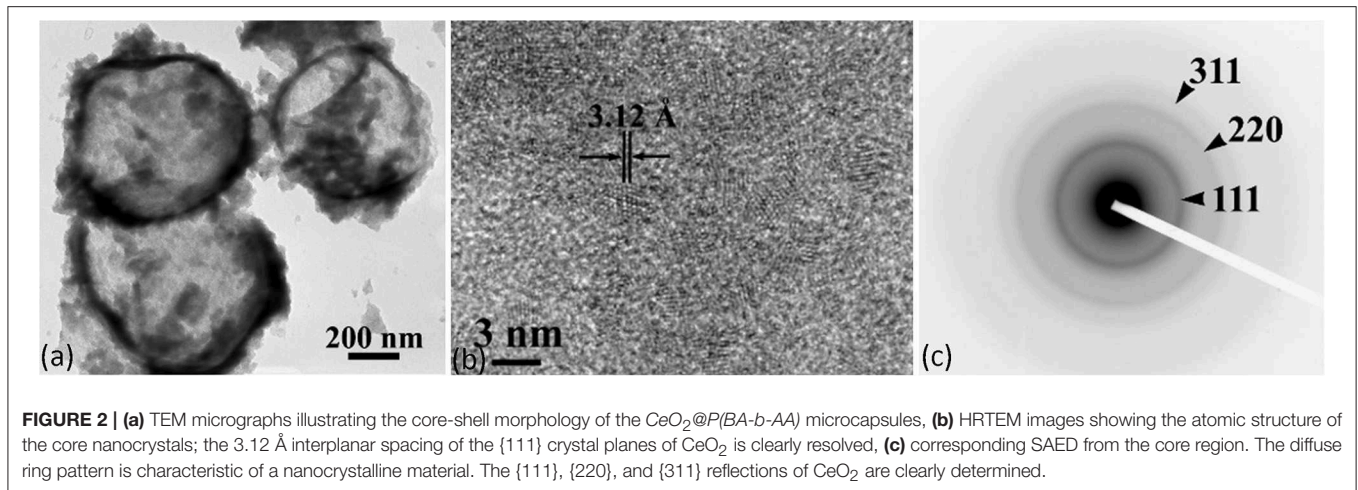


FIGURE 2 | (a) TEM micrographs illustrating the core-shell morphology of the $\text{CeO}_2@P(\text{BA-}b\text{-AA})$ microcapsules, (b) HRTEM images showing the atomic structure of the core nanocrystals; the 3.12 Å interplanar spacing of the {111} crystal planes of CeO_2 is clearly resolved, (c) corresponding SAED from the core region. The diffuse ring pattern is characteristic of a nanocrystalline material. The {111}, {220}, and {311} reflections of CeO_2 are clearly determined.

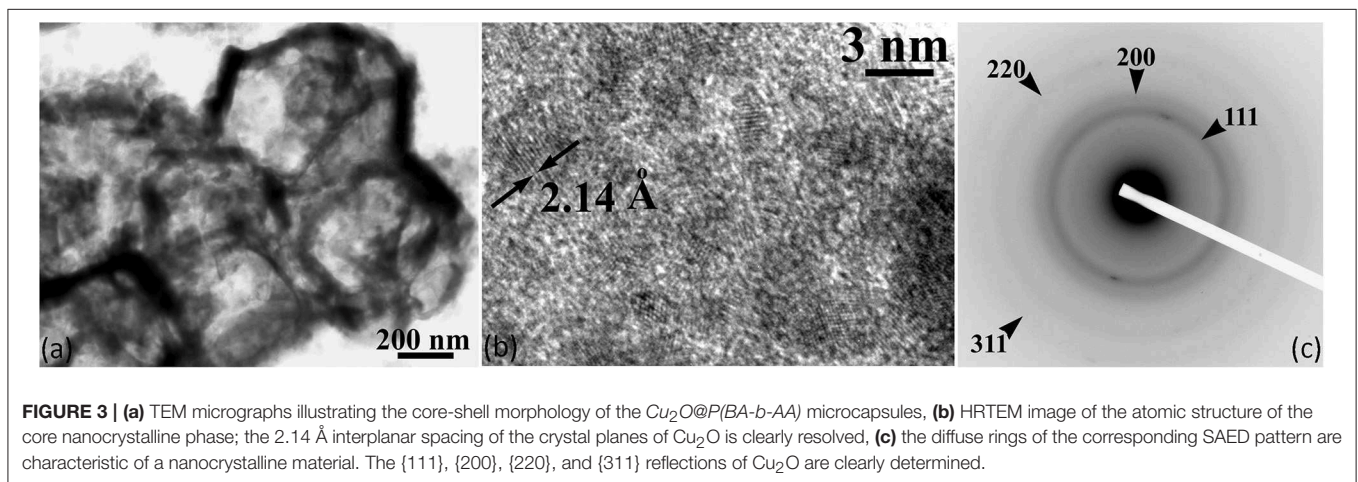


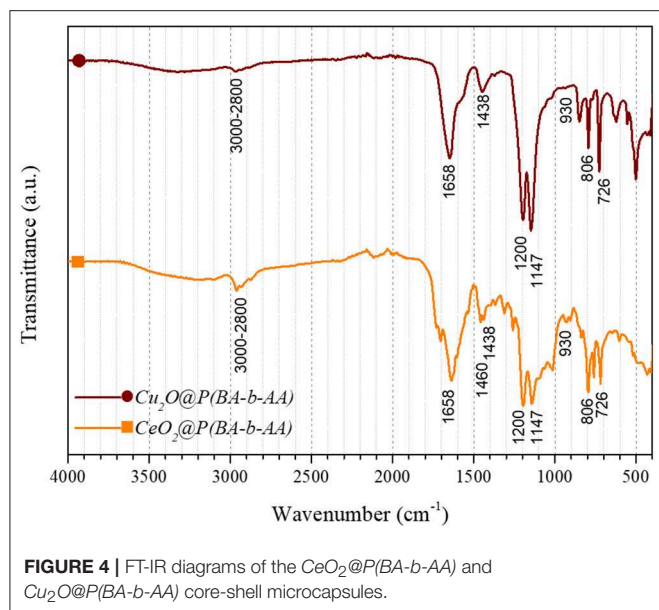
FIGURE 3 | (a) TEM micrographs illustrating the core-shell morphology of the $\text{Cu}_2\text{O}@P(\text{BA-}b\text{-AA})$ microcapsules, (b) HRTEM image of the atomic structure of the core nanocrystalline phase; the 2.14 Å interplanar spacing of the crystal planes of Cu_2O is clearly resolved, (c) the diffuse rings of the corresponding SAED pattern are characteristic of a nanocrystalline material. The {111}, {200}, {220}, and {311} reflections of Cu_2O are clearly determined.

explored by selected area electron diffraction (SAED) patterns (Figure 2c) and powder-XRD (Supplementary Figure S3). It can be seen that the diffuse ring pattern is characteristic of a nanocrystalline material. The {111}, {220}, and {311} reflections of CeO_2 are clearly determined. Taking into consideration Supplementary Figure S3, it was estimated that the core material is Cerianite (CeO_2) (PDF card #34-0394) crystallized in the face centered cubic structure and characterized by a lattice constant of 5.41 Å. The morphological and structural characteristics of the $\text{CeO}_2@P(\text{BA-}b\text{-AA})$ core-shell microcapsules are tabulated in Supplementary Table T2.

According to Figure 3a, spherical shapes of $\text{Cu}_2\text{O}@P(\text{BA-}b\text{-AA})$ microcapsules are observed with a core-shell configuration and average diameter of 670 ± 100 nm. The double shell is amorphous (dark contrast ring) and its average thickness is 70 ± 15 nm. The core comprises of the Cu_2O structure (lighter contrast) and exhibits a nanocrystalline phase with nanocrystals having a diameter range of 3–10 nm (Figures 3b,c), as illustrated by HRTEM and the corresponding SAED pattern. According to the HRTEM image of the atomic structure of the core nanocrystalline phase, the 2.14 Å

interplanar spacing of the crystal planes of Cu_2O is clearly resolved. Moreover, considering the diffuse rings of the corresponding SAED pattern it could be mentioned that they are characteristic of a nanocrystalline material. The {111}, {220}, and {311} reflections of Cu_2O are clearly determined. The core crystal structure is cubic with a lattice parameter equal to 4.27 Å. Supplementary Figure S4 illustrates the Cu_2O core powder-XRD where the {111}, {220}, and {311} diffraction peaks are clearly demonstrated. The morphological and structural characteristics of the $\text{Cu}_2\text{O}@P(\text{BA-}b\text{-AA})$ core-shell microcapsules are tabulated in Supplementary Table T3.

The successful synthesis of the polymer shell was confirmed through FT-IR analysis which revealed the characteristic adsorption peaks of poly(n-butyl acrylate; Figure 4). More specifically, in the region $3,000\text{--}2,800\text{ cm}^{-1}$ the C-H stretching vibrations arise and are more evident in the case of $\text{CeO}_2@P(\text{BA-}b\text{-AA})$ sample. The peaks at $2,970$ and $2,875\text{ cm}^{-1}$ are attributed to the asymmetric and symmetric stretching vibrations of the methyl group of PBA, respectively. A third intermediate peak at $2,930\text{ cm}^{-1}$ can be ascribed to the asymmetric C-H vibration of

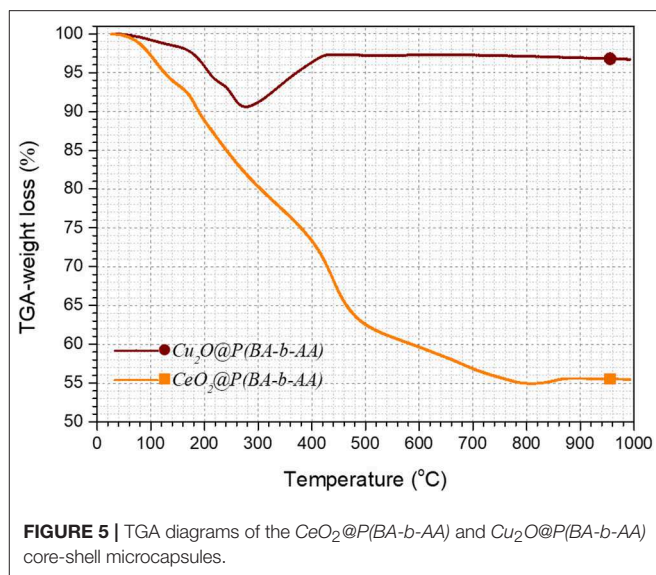


the methylene groups. These peaks are enhanced according to the increment in the polymer's crystallinity.

The broad adsorption peak at about $1,658\text{ cm}^{-1}$ refers to the stretching vibration of the carbonyl group ($C=O$) of PAA. The methylene bending mode vibration occurs at $1,460\text{ cm}^{-1}$ (main polymer chain), $1,438\text{ cm}^{-1}$, $1,395\text{ cm}^{-1}$ (n-butyl groups) and the CH_2 scissoring vibration at $1,454\text{ cm}^{-1}$ (polyacrylic acid). The two peaks at $1,373$ and $1,320\text{ cm}^{-1}$ correspond to the symmetric methyl bending mode and the C-H bending mode of the tertiary C-H groups, respectively.

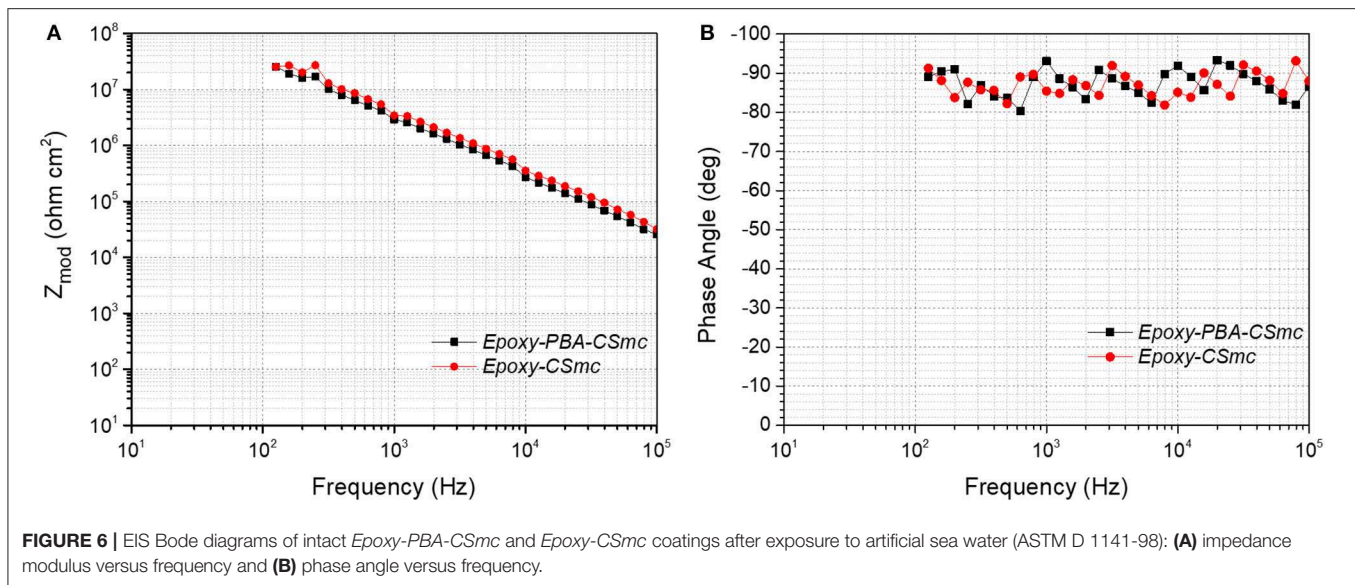
The C-O stretching mode shows two strong bands in the region $1,300\text{--}1,000\text{ cm}^{-1}$ in esters. In our case, the first adsorption band appears at $1,200\text{ cm}^{-1}$ and the second one at $1,147\text{ cm}^{-1}$. These bands are mainly attributed to asymmetrical and symmetrical C-O-C stretching modes of the n-butyl ester groups, respectively. Moreover, the doublet near 930 cm^{-1} is ascribed to the vibration corresponding to the n-butyl groups of the polymer and the skeletal stretching mode of the polymer main chain. The sharp band at 806 cm^{-1} also corresponds to the n-butyl groups. Finally, the double peaks at 767 and 726 cm^{-1} is due to the methylene rocking vibration mode (Kawasaki et al., 1961; Moharram et al., 2002; Moharram and Khafagi, 2007).

The thermal behavior of the synthesized polymer shell was investigated through TGA in N_2 atmosphere as illustrated in **Figure 5**. Taking into account the TGA diagram of the $Cu_2O@P(BA-b-AA)$ microcapsules, it may be remarked that in the temperature range between 30 and 170°C the diagram demonstrates a weight loss due to the evaporation of adsorbed water and the dehydroxylation process. Above this range, two parallel phenomena take place; the thermal decomposition of the PBA shell and the oxidation of the cuprous oxide core. A mass reduction is observed equal to $\sim 8\%$. On the other hand, a weight gain is observed over 600°C . The gain in weight did not exceed 7% of the initial mass, as seen from the TGA curve. This indicates that it is not stoichiometric with the amount of copper present



in the material. The most possible reaction is the oxidation of the cuprous oxide core to the thermodynamically more stable cupric oxide form (Sierra-Ávila et al., 2015), which overcomes the weight loss due to the polymer shell decomposition between 250 and 500°C (Li et al., 2006, 2015) due to the presence of gaseous contaminants within the N_2 gass as well as residual humidity in the material.

With respect to the $CeO_2@P(BA-b-AA)$ microcapsules (**Figure 5**) the sharp weight loss of 22% at 500°C is assigned to the polymeric shell decomposition. Over this temperature the thermal decomposition of other acetylacetonate-based metal complexes $[Me(acac)_z]$ suggest intermediate compound burning $[Ce(C_5H_7O_2)_2(CH_3COO)]$, $Ce(C_5H_7O_2)(CH_3COO)_2$, $Ce(OH)(CH_3COO)_3$, $CeO(CH_3COO)$, and $CeOCO_3$ prior to CeO_2 crystallization at 800°C , as reported in literature. A slight weight gain (0.5%) can be ascribed to the oxidation of Ce^{3+} to Ce^{4+} (Yao et al., 2003; Tania et al., 2008). Additionally, from equation (1) a grafting density of 1.5 chains/ nm^2 was calculated. The surface morphology of the produced coating systems was also evaluated. The surface top-viewed SEM images (**Supplementary Figures S5a,b**) reveal no defects or cracks can be spotted on the corrosion protective coating systems, *Epoxy-PBA-CSmc* and *Epoxy-CSmc*, respectively. In **Supplementary Figures S6a,b** the topographic maps of the average coating thicknesses of the *Epoxy-PBA-CSmc* and *Epoxy-CSmc*, respectively, corrosion protective coating systems measured through induction method reveal an increment corresponding on the bottom side of the samples; an observation commonly presented when a baker film applicator is utilized. For consistency reasons, all the electrochemical characterizations were conducted on the middle zone of the coated HDG substrates. The cross-section SEM image of *Epoxy-PBA-CSmc* (**Supplementary Figure S7a**) illustrates the coating thickness measurements which were found equal to $44 \pm 3\ \mu\text{m}$, and $90 \pm 3\ \mu\text{m}$ for the two layers, respectively. Moreover, the cross-section SEM image of *Epoxy-CSmc* is



depicted in **Supplementary Figure S7b** where it can be seen that the thickness of the two layers is $30 \pm 3 \mu\text{m}$ and $114 \pm 3 \mu\text{m}$, respectively.

Electrochemical Studies

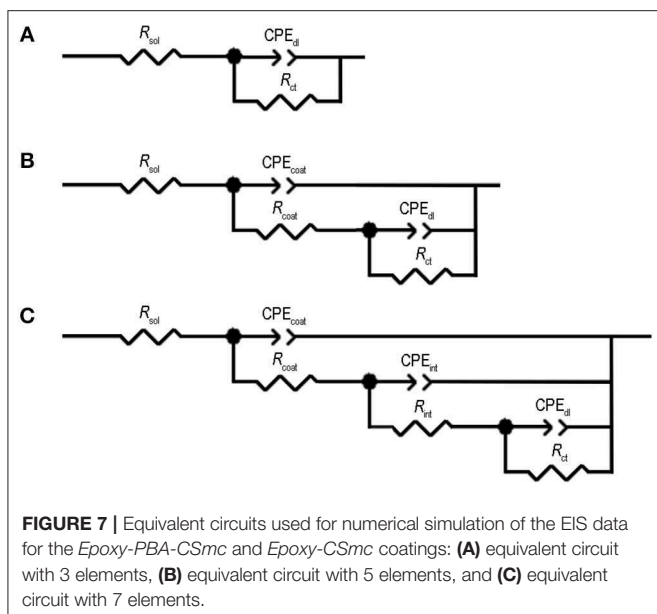
EIS is used as a powerful tool to investigate the barrier properties of the coating systems developed in the current study and to assess the impact of the addition of a liquid rubber polymer either as a container surface modified or as an additive incorporated in free form in the epoxy matrix. As it has been well-documented previously in literature, the magnitude of impedance modulus at low frequency ($|Z|_{0.01 \text{ Hz}}$) can be used to assess the overall anti-corrosive behavior of an organic coating system, while the charge transfer resistance (R_{ct}) indicates the resistance to a flow of charge, electronic or ionic, which is inversely proportional to the corrosion rate underneath the coating and its enhancement is associated with self-healing effects (Zhang et al., 2004; Zheludkevich, 2009; Borisova et al., 2013; Meng et al., 2015; Njoku et al., 2017; Ubaid et al., 2019).

Figure 6 illustrates the Bode diagrams of (a) the impedance plot vs. frequency and (b) the phase angle diagram vs. the frequency resulting from the exposure of intact coatings to artificial sea water (ASTM D 1141-98) over a period of 223 days. It is observed that in all spectra, both intact coatings are characterized by the presence of a capacitive response during their exposure to the highly corrosive environment for a period of 223 days. The intact coatings reveal a time constant that is at the high frequencies, characteristic of the increased anticorrosive protection they provide to the substrate. In particular, the capacitive behavior of the coatings is shown at high frequencies. The phase angle of the system is between -80° and -90° in the measured frequency range for all immersion time, revealing that the coatings behave as a capacitor. This behavior implies that the coatings are characterized by good barrier properties and behave as an insulator by isolating the metal surface from the corrosive

environment (Cabral et al., 2006; Trabelsi et al., 2006; Foyet et al., 2013; Qiao et al., 2015).

Supplementary Figures S8, S9 show the evolution of impedance spectra of the two artificially scribed coatings after exposure to 5 mM NaCl solution. The impedance spectra evolution of scribed *Epoxy-PBA-CSmc* after exposure to 5 mM NaCl solution are illustrated in **Supplementary Figure S8a**. The coating showed stable impedance values for 1 to 4 h of immersion to the corrosive electrolyte, equal to $470 \text{ k}\Omega \text{ cm}^2$. After 96 h of immersion, the impedance value $|Z|_{0.01 \text{ Hz}}$ increased to $670 \text{ k}\Omega \text{ cm}^2$. The scribed *Epoxy-PBA-CSmc* reveals three time constants from the beginning of immersion (**Supplementary Figure S8b**). The one in the high frequency range can be attributed to the coating due to the fact that the exposed area includes the scribe together with a part of the coating, a second small one in the middle frequency range can be ascribed to the response of processes occurring at the coating/ substrate interface and a third time constant in the low frequency range due to the corrosion process at the metallic surface. EIS Bode plots of scribed *Epoxy-CSmc* are depicted in **Supplementary Figure S9a**. The coating presents a progressively increase of the magnitude of impedance modulus at low frequency ($|Z|_{0.01 \text{ Hz}}$) from $56 \text{ k}\Omega \text{ cm}^2$ at 7 h to $130 \text{ k}\Omega \text{ cm}^2$ after 96 h of exposure to the electrolyte. The *Epoxy-CSmc* reveals three time constants for all time intervals till 96 h of immersion (**Supplementary Figure S9a**). The overall impedance values revealed that the presence of the liquid rubber addition in free form (*Epoxy-PBA-CSmc*) improves the charge transfer resistance of the epoxy-based coating system including microcapsules with cerium-ions resulting in higher impedance values after defect formation.

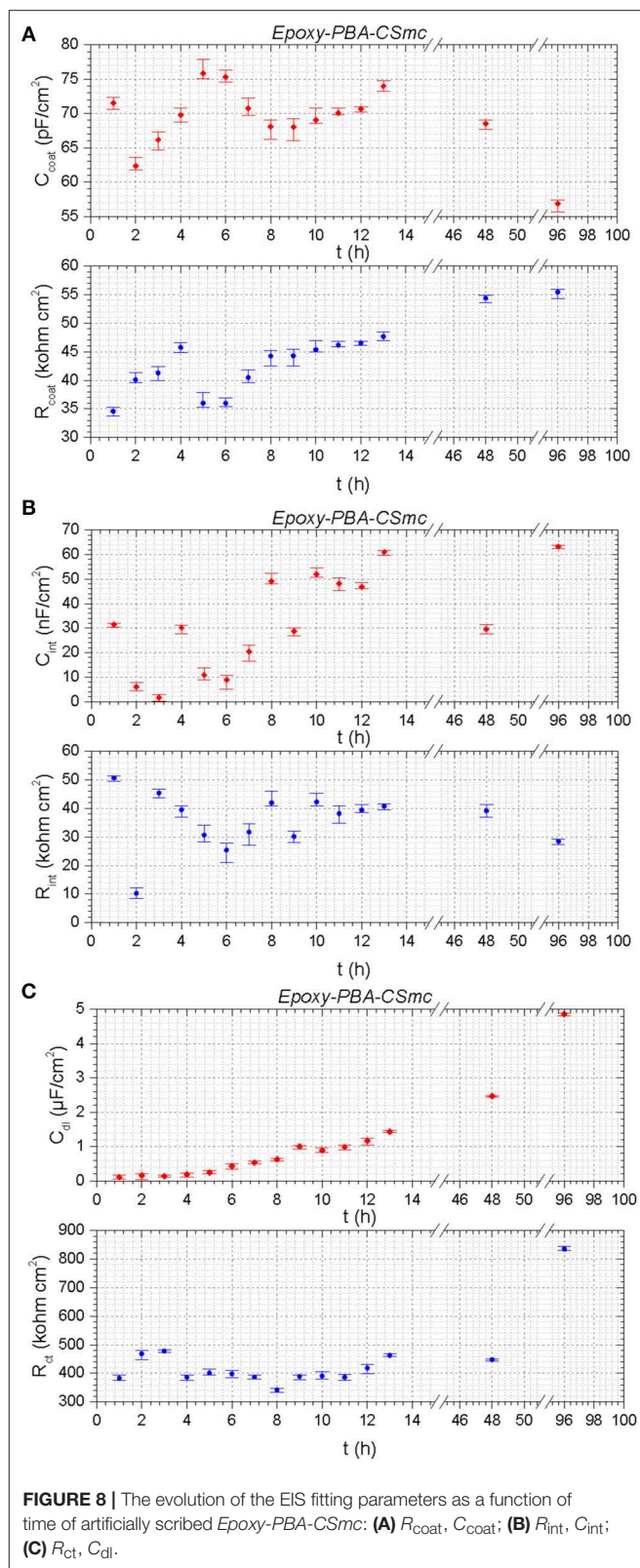
The EIS results of the artificially scribed *Epoxy-PBA-CSmc* and *Epoxy-CSmc* coatings were fitted using the equivalent electric circuit of **Figure 7C**. The equivalent electric circuit of **Figure 7C** includes seven elements and corresponds to an EIS spectrum comprising of three time constants. In particular, it consists of



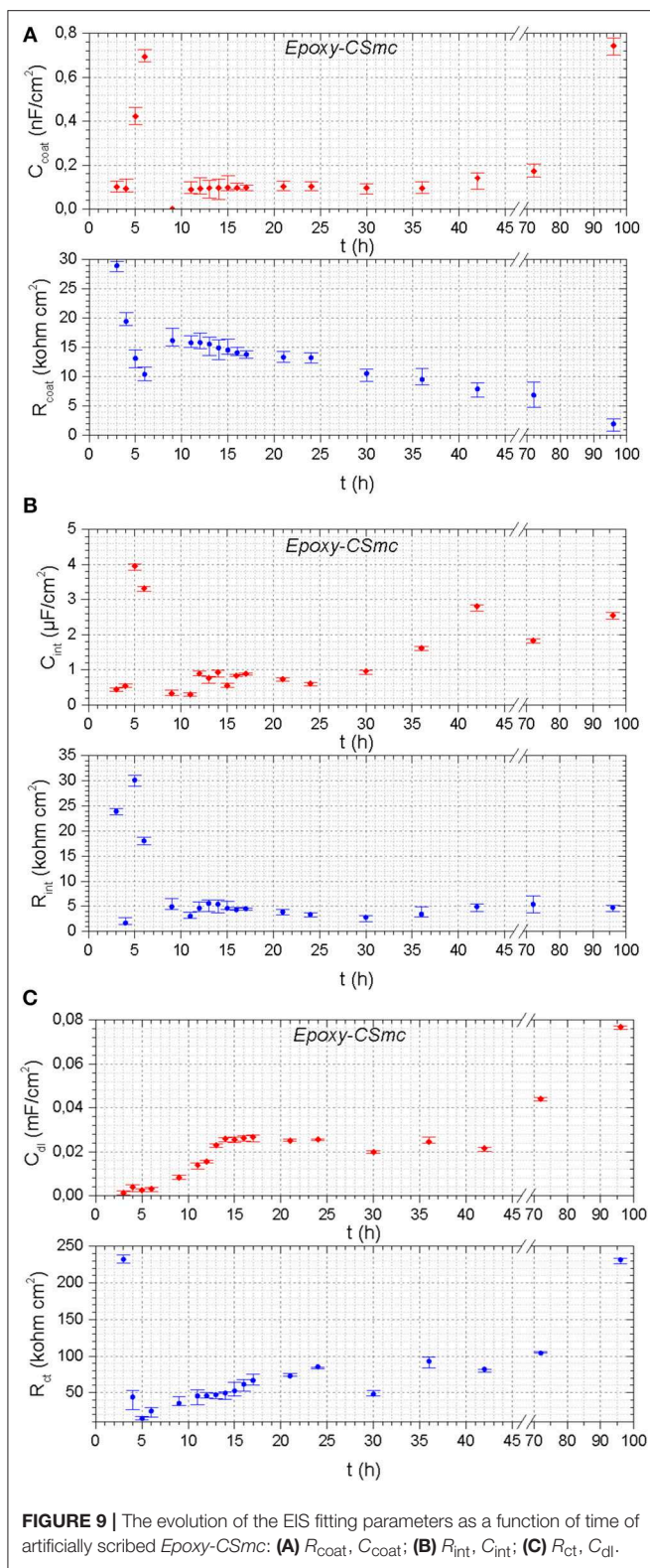
the resistance of the solution (R_{sol}), the pore resistance and the CPE of the coating ($R_{coat} - CPE_{coat}$) in parallel connection that are attributed to the response of the electrolyte inside the pores of the coating, the interface resistance and the interface CPE ($R_{int} - CPE_{int}$) that are assigned to the response of the presence of electrolyte at the oxide layer and finally, the charge transfer resistance and the double-layer CPE ($R_{ct} - CPE_{dl}$) that are due to the presence of corrosion active pits at the oxide-metallic substrate interface.

Taking into account the aforementioned Equation (3), the C_{coat} , C_{int} , C_{dl} parameters were calculated. **Figures 8, 9** illustrate the evolution of C_{coat} , C_{int} , C_{dl} , R_{coat} , R_{int} , R_{ct} as a function of time in 5 mM NaCl for both the artificially scribed *Epoxy-PBA-CSmc* and *Epoxy-CSmc* coatings, respectively (**Supplementary Table T4**).

The fitting results for the scribed *Epoxy-PBA-CSmc* reveal relatively small fluctuations on R_{coat} and C_{coat} , which indicate a stable performance of the coating during immersion in the corrosive environment (**Figure 8A**). In detail, the pore resistance of the coating increases till the 4 h of exposure, while it suffers from a sudden drop at the 5 and 6 h, with a corresponding increment in the coating capacitance values (C_{coat}). After 7 h and till the fourth day of exposure (96 h) the pore resistance shows a continuous enhancement, while the corresponding capacitance is decreased. The values for the pore resistance and capacitance reflect the evolution of the barrier properties of the system and the decreasing number of conductive ways from the electrolyte to the substrate (Montemor et al., 2008; Plawecka et al., 2014). The R_{ct} values present a progressive increment after 8 h of immersion (**Figure 8C**), while at the same time interval the interlayer resistance (R_{int}) is also increased, indicating the formation of a stable protective oxide layer (**Figure 8B**). The overall recovery of R_{ct} value increased 144% from the first till the 96th hour of immersion, from 341.53 to 834.7 kΩ cm², respectively (Ubaid et al., 2019).



The pore resistance (R_{coat}) for the scribed *Epoxy-CSmc* continuously decreases as the immersion time elapses and the corresponding capacitance values (C_{coat}) continue to increase,



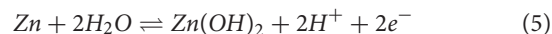
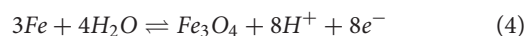
indicating the progressive damage of the coating due to successive electrolyte ingress (Figure 9A). The smallest R_{ct} value is observed at the 5 h after which an improvement follows till the 96 h of exposure (Figure 9C). The recovery of the charge transfer

resistance from the smallest value observed is equal to 1,465% (Ubaid et al., 2019; increased from 14.8 to 231.71 $k\Omega\text{ cm}^2$).

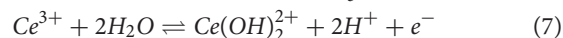
Concluding, in both studied systems, the charge transfer resistance is decreased after the contact with the corrosive environment, yet the values are recovered to some point due to the beneficial effect of cerium-based additives.

In general, the literature agrees that rare earths behave as cathodic corrosion inhibitors for many metal alloys when added to a corrosive electrolyte (de Damborenea et al., 2014; Hughes et al., 2014; O’Keefe et al., 2014; Yasakau et al., 2014). In particular, the process of inhibiting corrosion through the lanthanide salts for various materials is a consequence of the inhibition of cathodic regions by the precipitation of an oxide/hydroxide film. This was first mentioned by Hinton in 1984 and shortly afterwards in his own bibliographic review in 1992 (Hinton, 1992).

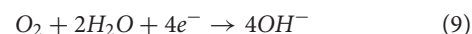
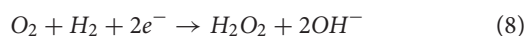
Iron and zinc undergo severe localized dissolution at a number of anodic sites forming hydroxides of limited solubility according to the following equations (Pourbaix and de Zoubov, 1966):



Trivalent ions of rare earths in an aqueous environment undergo gradual hydrolysis and form complexed hydroxylated ions, as shown in Equation (7), and for Ce in Equation (8).



The exact chemical composition of these compounds depends on the type of the lanthanide cation added to the medium and the specific anion of the solution. This complex precipitates and results in the formation of a hydroxide layer as the pH of the solution locally increases at the cathodic areas, where the main reaction is the reduction of oxygen (Equations 9, 10).



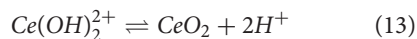
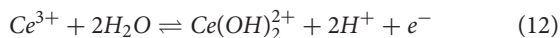
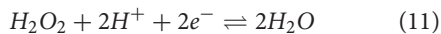
Which of these two reaction pathways predominates, depends on the composition of the metal substrate and the presence, or absence, of any surface oxide film (Bockris and Khan, 1993).

The rare earth hydroxides formed are stable in alkaline solutions and dissolve under acidic conditions. The critical pH values at which the hydroxides precipitate is a function of the concentration of the trivalent ion (Ce^{3+}), which cannot be assumed or calculated in our case (de Damborenea et al., 2014).

Additionally, as shown in related works, in the case of zinc, the gradual dissolution occurring in the early stages of immersion is altered due to the adsorption of cerium ions. According to Aramaki and Arenas and de Damborenea cerium will react with the hydroxylated surface of the metal, thus impeding adsorption of the chlorides. Then, a complex is formed on the metallic surface such as $[Zn]OCe(III)OH_2$ acting as a precursor to form the corrosion inhibiting layer. In addition, the precipitation of $Ce(OH)_3$ in the cathodic regions is favored due to the lower

solubility compared to zinc hydroxide (1.6×10^{-20} and 7.28×10^{-17} ; Aramaki, 2001; Arenas and de Damborenea, 2006).

A conflicting issue in literature is related with the oxidative state of the cerium ions found in the film. In detail, some claim that both oxygen and hydrogen peroxide (as produced by Equation 9) can act as oxidizing agents producing Ce^{4+} and CeO_2 , as shown by the following reactions (Equations 7–10)



Although in the present study no local pH measurement techniques and electrode potential measurements were utilized, according to literature (Böhm et al., 2000), a pH equal to 8.7 is needed in order Ce^{3+} to be oxidized to Ce^{4+} (giving $Ce(OH)_2^{2+}$) for air-equilibrated water at ambient pressure ($p_{O_2} = 0.2$ atm), but no direct oxidation of $Ce(OH)_3$ to CeO_2 is possible in any pH value. In any case, the pH values needed for the formation of Ce^{4+} by oxidation caused by hydrogen peroxide, are above 10, which is unlikely under our experimental conditions (pH ranging from 6 to 9). In addition, according to Hinton and Wilson (Hinton and Wilson, 1989), it is unlikely that all Ce^{3+} will be oxidized because H_2O_2 is only formed as an intermediate product of the oxygen reduction reaction.

In other related works, it is said that hydrogen peroxide presence contributes to the oxidation of Ce^{3+} to Ce^{4+} , promoting the formation of oxides and hydroxides from both species, under prolonged time exposure conditions (Thierry et al., 1991; Aramaki, 2002a,b). Given the above, it is assumed that the first step in the deposition of a Ce-rich film under our particular experimental conditions is the precipitation of $Ce(OH)_3$ which may subsequently react with CO_2 from the air to form carbonates. The formation of a stable Ce-rich film is confirmed by elemental mapping EDS results on the blocked scribe area with precipitated products after the exposure to the corrosive electrolyte (Figure 10).

It is also reported in literature that the reaction between amine and epoxy groups is catalyzed by increased pH producing a new protective film (Kartsonakis et al., 2012). Another parameter positively affecting the protective performance of the studied systems after scratch formation is the incorporation of the polymer-modified microcapsules which promote the compatibility with the epoxy resin matrix and enhance the consistency of the coating matrix due to the reaction of hydroxyl groups of the PAA block of the polymer shell with the epoxide rings of the epoxy resin (Soares and Livi, 2017).

Effect of Thermally-Induced Defect Closure on Barrier Properties

In the current study, a low T_g liquid rubber elastomer was used in order to add a second self-healing mechanism into the coatings. The polymer which was incorporated either as a surface modification of the microcapsules or as a polymer in free form is expected to modify the T_g of the system. The main aim is to

induce self-healing of an artificial scribe upon heating the film above its T_g , where the polymeric chains have enhanced mobility. In this way, the deformation can be cured, possibly affecting positively and restoring the corrosion protection performance of the under-study film. Thus, the term “self-healing” is related with the recovery of the anti-corrosion protection of a coating system after being damaged due to a non-autonomous self-healing mechanism triggered by temperature. Theoretically, if the ratio between the defect size and the coating thickness is smaller than one, the aforementioned recovery may be complete and repeatable (D’Hollander et al., 2009; Jorcin et al., 2010; Luo and Mather, 2013).

Figures 11, 12 illustrate the morphology of the scribed coatings before and after thermal treatment at $90^\circ C$ for 30 min, along with the line elemental EDS analysis of the main chemical elements of the metallic substrate (Fe, Zn) and the coating (C).

The separated crack surfaces are in spatial proximity after heating for samples *Epoxy-PBA-CSmc* and *Epoxy-CSmc*. The transition from a glassy to a fluid state is based on the onset of molecular motion within the polymer chains. In the region of T_g , and above, the polymer softens and the modulus of elasticity decreases by 3 orders of magnitude and the polymer switches to an elastic state (Souza and Reis, 2013). The potential crack re-bonding cannot be easily visualized due to crack closure. Thus, EIS is again used to assess the functional self-healing, which in the current study is the partial restoration of the barrier properties. Supplementary Figure S10 represents the EIS Bode results of the scribed *Epoxy-PBA-CSmc* and *Epoxy-CSmc* coatings after their exposure for 1 h into 5 mM NaCl, before and after heat-induced healing. The results were also numerically fitted to quantitatively assess the coatings protective performance after heat treatment (Table 3). One relaxation time is observed for both coatings before their exposure to temperature that is described by the equivalent circuit of Figure 7A. The R_{sol} refers to the electrolyte resistance, CPE_{dl} refers to the CPE of the double layer and R_{ct} is the charge transfer resistance. Both CPE_{dl} and R_{ct} are associated to the corrosion process. On the other hand, two time constants are evident for both coatings after their thermal treatment. In the equivalent circuit (Figure 7B) the pore resistance R_{coat} is combined with a CPE element (CPE_{coat}) to account for the response of the electrolyte inside the pores of the coating and the R_{ct} is associated with the double layer CPE (CPE_{dl}). It should be mentioned that the presence of two time constants indicates that there is no sufficient re-bonding of the two separated surfaces of the artificial defect and an imperfect self-healing action. Additionally, the corrosion process underneath the scratched films has already initiated during immersion in the electrolyte, which explain the presence of two time constants. The corresponding EIS Nyquist plots (Supplementary Figure S11) confirm the aforementioned results. The increment of the charge transfer resistance from 2.04 to 102.9 $k\Omega\ cm^2$ suggests a recovery of 4.944% for *Epoxy-PBA-CSmc* (Table 3). Thus, the polarization resistance or the corrosion reactions at the HDG surface is partially suppressed. Moreover, the fitting results for *Epoxy-CSmc* reveal that the charge transfer resistance is also increased from 4.77 to 234.1 $k\Omega\ cm^2$, clearly denoting a recovery of 4.807%

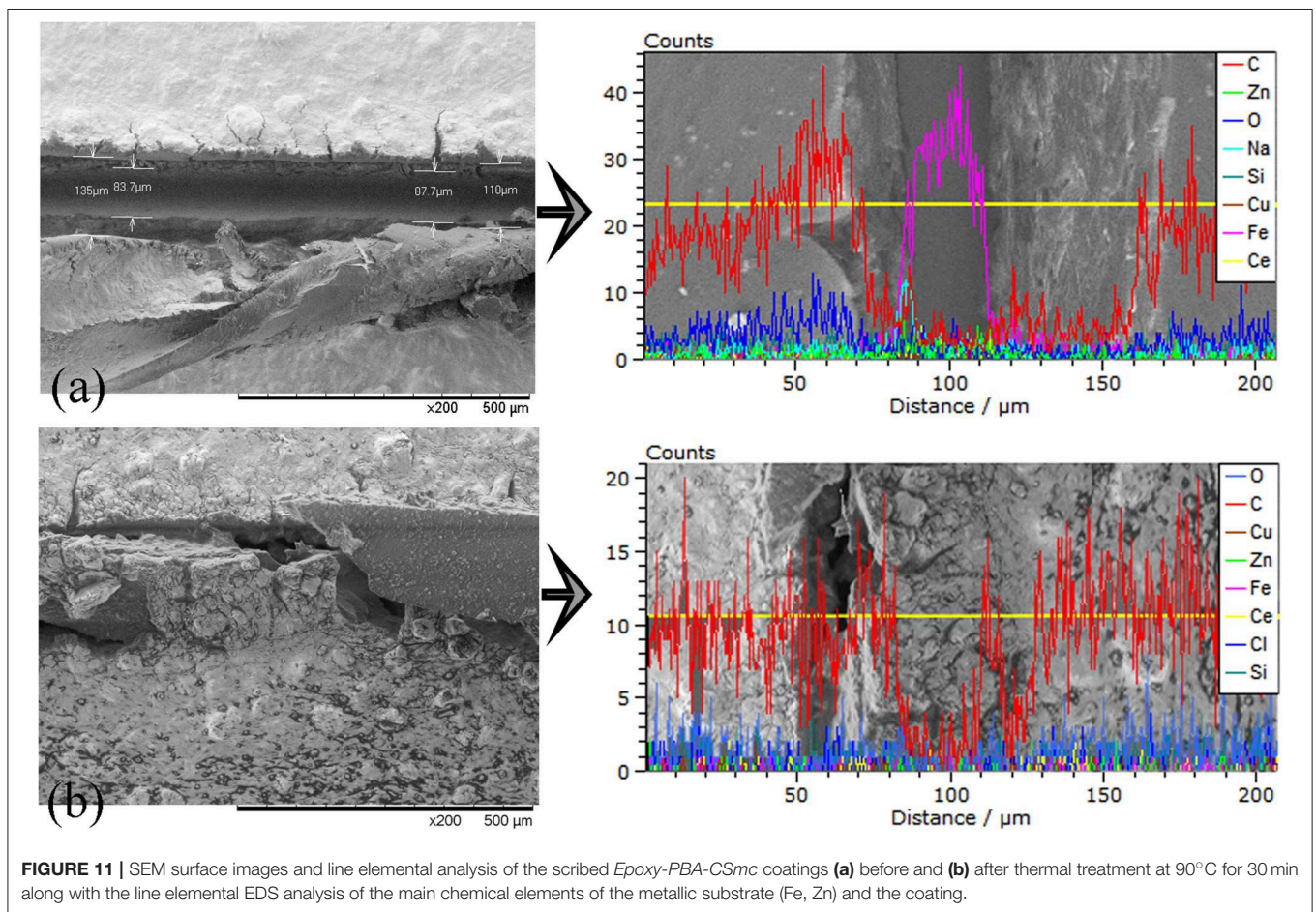
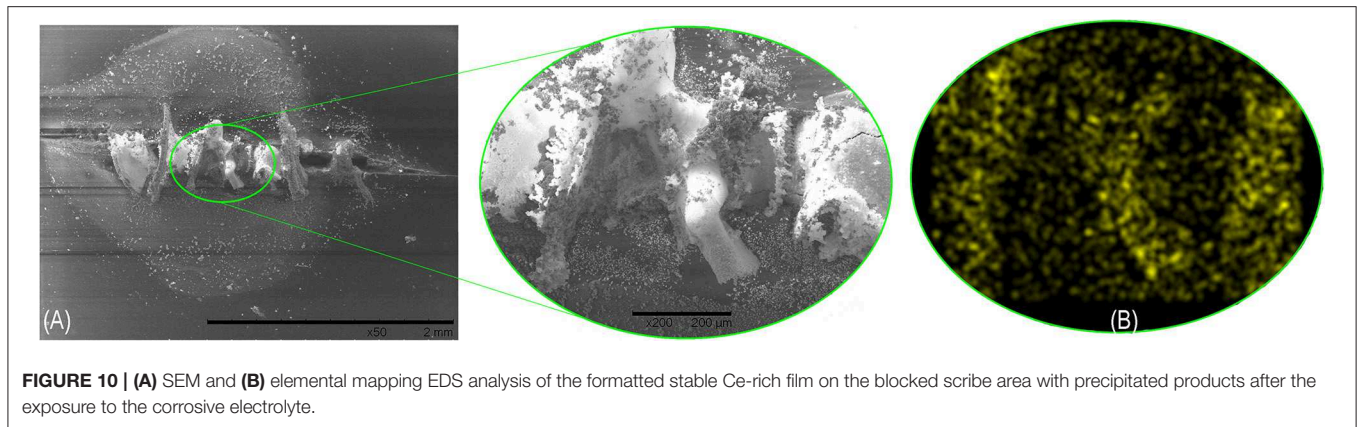


(Table 3). The results for Epoxy-CSmc further confirm the observation through SEM that there is also a material reflow in the defect's area where the metallic substrate was exposed, indicating re-bonding between the HDG steel and the liquid rubber polymer.

To conclude, the EIS measurements showed that the liquid rubber addition either in free form (Epoxy-PBA-CSmc) or in the presence of the core-shell microcapsules, improved the charge transfer resistance of the coating systems,

indicating a partial inhibition of the corrosion process on HDG substrate, after thermal exposure above its T_g . This is also supported by the DSC measurements conducted on Epoxy-PBA-CSmc coating (Supplementary Figure S12), which revealed a reduction of the T_g of the system ($T_g = 79^\circ\text{C}$) due to the elastomer addition, in comparison to the theoretical T_g values of its main epoxy-based component (122°C for bisphenol A diglycidyl ether—diethylenetriamine cured; Bryan Ellis, 2000).

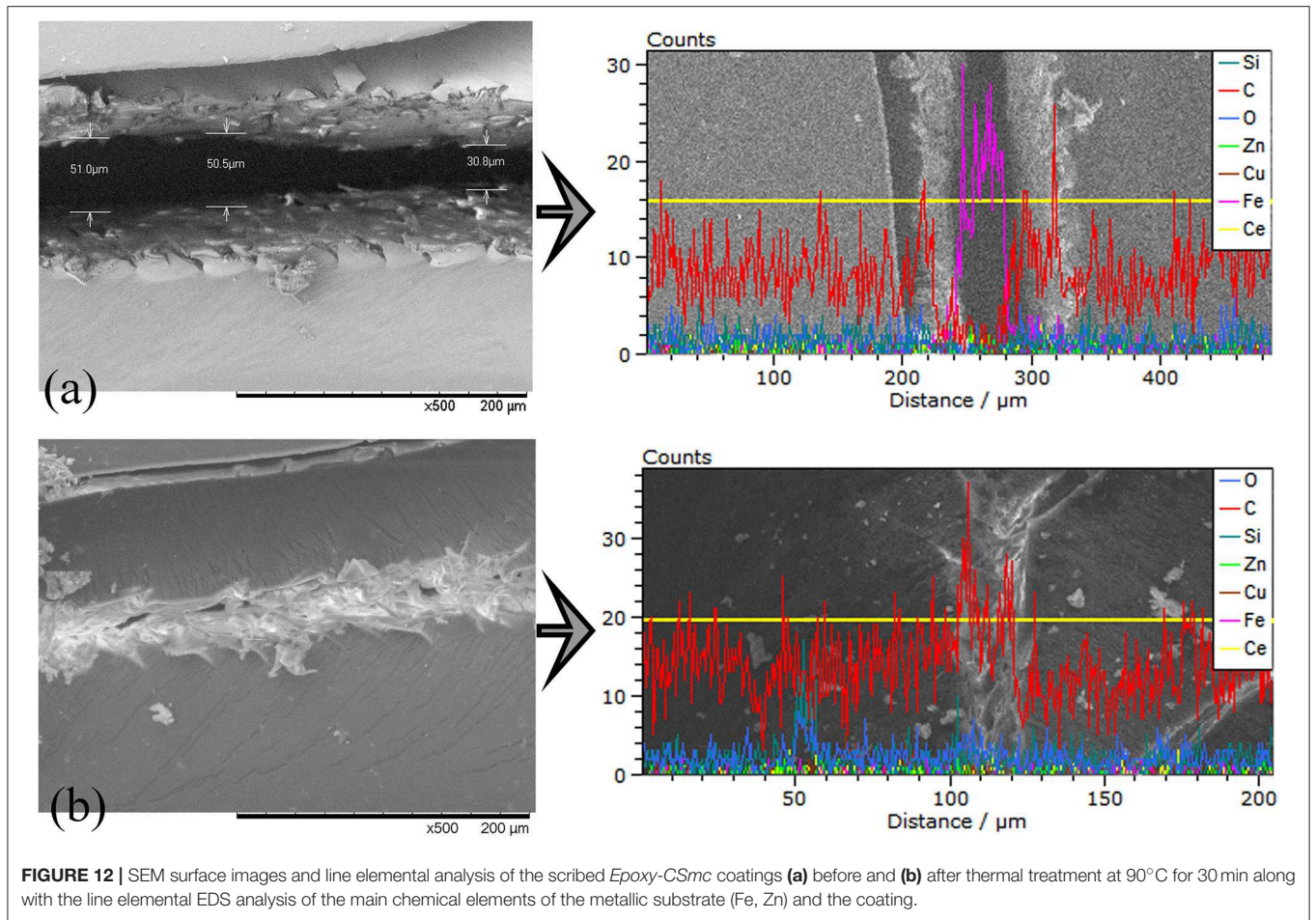


TABLE 3 | Fitting parameters according to equivalent circuits of **Figures 7A,B** of the scribed *Epoxy-PBA-CSmc* and *Epoxy-CSmc* coatings after their exposure for 1 h into 5 mM NaCl, before and after heat-induced healing.

	<i>Epoxy-PBA-CSmc</i> before	<i>Epoxy-PBA-CSmc</i> after	<i>Epoxy-CSmc</i> before	<i>Epoxy-CSmc</i> after
CPE_{coat-T} (nF cm ⁻² s ⁻ⁿ)	–	0.13	–	1.79
Error (%)	–	15.7	–	50.0
CPE_{coat-P}	–	0.97422	–	0.75727
Error (%)	–	1.36	–	5.46
R_{coat} (kohm cm ²)	–	37.3	–	36.4
Error (%)	–	0.85	–	5.99
C_{coat} (nF cm ⁻²)	–	903.3	–	814.1
CPE_{dl-T} (μF cm ⁻² s ⁻ⁿ)	25.5	1.27	1.52	0.13
Error (%)	2.56	4.91	6.69	8.92
CPE_{dl-P}	0.68035	0.63769	0.73103	0.76513
Error (%)	0.57	1.76	1.18	2.06
R_{ct} (kohm cm ²)	2.04	102.9	4.77	234.1
Error (%)	0.71	1.68	0.85	2.07
C_{dl} (μF cm ⁻²)	6.36	0.40	0.24	0.05
Chi-squared	0.00237	0.00299	0.00833	0.01198

CONCLUSION

Two advanced coating systems have been presented in this work incorporating a type of core-shell cerium-based microcapsules which were compared with an epoxy-based coating including cerium microcapsules. The main aim was to investigate the influence of a liquid rubber polymer addition either as a surface-modifier or as an additive in free form on the anti-corrosion protection offered and their potentially heat-triggered material re-flow/self-healing ability.

The first autonomous self-healing mechanism refers to the well-known and studied anti-corrosion effect of cerium-based containers that contribute to the formation of stable chelating complexes on the surface of galvanized steel. On the other hand, their polymer-based surface modification enhanced the interaction of the microcapsules' surface with the epoxy matrix and the overall EIS response upon defect formation.

With the addition of a liquid rubber polymer in free form it is possible to incorporate a second, non-autonomous mechanism which was studied and presented in this work based on activation by increasing the temperature to values higher than the T_g of the coating system. In this case, except from the material re-flow ability of the system also shown in the coating incorporating the core-shell microcapsules, the protection performance of the coating is increased, offering a partial suppression of the underlying corrosion process.

Future plans of the current work include localized impedance spectroscopy measurements for the assessment of the local electrochemical corrosion reaction under the artificially scribed coating, along with complementary antifouling performance evaluation.

DATA AVAILABILITY

The datasets generated for this study are available on request to the corresponding author.

AUTHOR CONTRIBUTIONS

EK and IK conceived, designed and performed the analysis. EK collected the data and wrote the paper. IK performed the Scanning Electron Microscopy Analysis and also contributed during the experiments and the data analysis. CC had the overall responsibility for the final manuscript and contributed with critical comments and suggestions during the experimental process.

REFERENCES

- Abdolah Zadeh, M., van der Zwaag, S., and García, S. J. (2016). Assessment of healed scratches in intrinsic healing coatings by AC/DC/AC accelerated electrochemical procedure. *Surf. Coat. Technol.* 303, 396–405. doi: 10.1016/j.surfcoat.2015.11.001
- Aramaki, K. (2001). The inhibition effects of cation inhibitors on corrosion of zinc in aerated 0.5 M NaCl. *Corros. Sci.* 43, 1573–1588. doi: 10.1016/S0010-938X(00)00144-X

SUPPLEMENTARY MATERIAL

The Supplementary Material for this article can be found online at: <https://www.frontiersin.org/articles/10.3389/fmats.2019.00222/full#supplementary-material>

Supplementary Figure S1 | Schematic representation of the synthesis of the diblock copolymer onto the surface of either CeO_2 or Cu_2O .

Supplementary Figure S2 | SEM surface images and line elemental EDS analysis of the artificially scribed: (a) *Epoxy-PBA-CSmc* and (b) *Epoxy-CSmc* coating systems.

Supplementary Figure S3 | XRD pattern of the $CeO_2@P(BA-b-AA)$ core-shell microcapsules.

Supplementary Figure S4 | XRD pattern of the of the $Cu_2O@P(BA-b-AA)$ core-shell microcapsules.

Supplementary Figure S5 | SEM surface images of the: (a) *Epoxy-PBA-CSmc* and (b) *Epoxy-CSmc* corrosion protective coating systems.

Supplementary Figure S6 | Topographic maps with the average coating thicknesses of the: (a) *Epoxy-PBA-CSmc* and (b) *Epoxy-CSmc* corrosion protective coating systems.

Supplementary Figure S7 | SEM cross-section images of the coating thicknesses of the: (a) *Epoxy-PBA-CSmc* and (b) *Epoxy-CSmc* corrosion protective coating systems.

Supplementary Figure S8 | EIS Bode diagrams of artificially scribed *Epoxy-PBA-CSmc* after exposure to 5 mM NaCl solution: (a) Impedance modulus versus frequency and (b) Phase angle versus frequency.

Supplementary Figure S9 | EIS Bode diagrams of artificially scribed *Epoxy-CSmc* after exposure to 5 mM NaCl solution: (a) Impedance modulus versus frequency and (b) Phase angle versus frequency.

Supplementary Figure S10 | EIS Bode diagrams of artificially scribed *Epoxy-PBA-CSmc* and *Epoxy-CSmc* coatings, before and after heat-induced healing after exposure to 5 mM NaCl solution: (a) Impedance modulus versus frequency and (b) Phase angle versus frequency.

Supplementary Figure S11 | EIS Nyquist diagrams of artificially scribed *Epoxy-PBA-CSmc* and *Epoxy-CSmc* coatings, before and after heat-induced healing after exposure to 5 mM NaCl solution.

Supplementary Figure S12 | The DSC measurements conducted on the scribed *Epoxy-PBA-CSmc* coating after thermal treatment at 90°C for 30 min.

Supplementary Table T1 | Chemical Composition of Substitute Ocean Water (according to ASTM D1141-98).

Supplementary Table T2 | The morphological and structural characteristics of the $CeO_2@P(BA-b-AA)$ core-shell microcapsules.

Supplementary Table T3 | The morphological and structural characteristics of $Cu_2O@P(BA-b-AA)$ core-shell microcapsules.

Supplementary Table T4 | Fitting parameters according to equivalent circuit of **Figure 7C** after samples exposure to 5 mM NaCl solution.

Aramaki, K. (2002a). Preparation of chromate-free, self-healing polymer films containing sodium silicate on zinc pretreated in a cerium(III) nitrate solution for preventing zinc corrosion at scratches in 0.5 M NaCl. *Corros. Sci.* 44, 1375–1389. doi: 10.1016/S0010-938X(01)00138-x

Aramaki, K. (2002b). Self-healing mechanism of an organosiloxane polymer film containing sodium silicate and cerium(III) nitrate for corrosion of scratched zinc surface in 0.5 M NaCl. *Corros. Sci.* 44, 1621–1632. doi: 10.1016/S0010-938X(01)00171-8

- Arenas, M. A., and de Damborenea, J. (2006). Interference by cerium cations during the multi-step zinc dissolution process in a chloride-containing electrolyte. *Corros. Sci.* 48, 3196–3207. doi: 10.1016/j.corsci.2005.10.015
- Bagheri, R., Marouf, B. T., and Pearson, R. A. (2009). Rubber-toughened epoxies: a critical review. *Polym. Rev.* 49, 201–225. doi: 10.1080/15583720903048227
- Balaskas, A. C., Hashimoto, T., Curioni, M., and Thompson, G. E. (2017). Two-shell structured PMAA@CeO₂ nanocontainers loaded with 2-mercaptobenzothiazole for corrosion protection of damaged epoxy coated AA 2024-T3. *Nanoscale* 9, 5499–5508. doi: 10.1039/c7nr00858a
- Barsoukov, E., and Macdonald, R. J. (2018). *Impedance Spectroscopy Theory Experiment and Applications*. Hoboken, NJ: John Wiley and Sons Inc., Publication, 13–20.
- Benoit, D. N., Zhu, H., Lilierose, M. H., Verm, R. A., Ali, N., Morrison, A. N., et al. (2012). Measuring the grafting density of nanoparticles in solution by analytical ultracentrifugation and total organic carbon analysis. *Anal. Chem.* 84, 9238–9245. doi: 10.1021/ac301980a
- Bockris, J. O. M., and Khan, S. U. M. (eds.). (1993). "Surface electrochemistry," in *A Molecular Level Approach*, eds J. O'M. Bockris and S. U. M. Khan (Boston, MA: Springer), 764–770.
- Böhm, S., Greef, R., McMurray, H. N., Powell, S. M., and Worsley, D. A. (2000). Kinetic and mechanistic studies of rare earth-rich protective film formation using *in situ* ellipsometry. *J. Electrochem. Soc.* 147, 3286. doi: 10.1149/1.1393897
- Borisova, D., Akçakayran, D., Schenderlein, M., Möhwald, H., and Shchukin, D. G. (2013). Nanocontainer-based anticorrosive coatings: effect of the container size on the self-healing performance. *Adv. Funct. Mater.* 23, 3799–3812. doi: 10.1002/adfm.201203715
- Bryan Ellis, R. S. (2000). *Polymers - A Property Database*. Boca Raton, FL: CRC Press.
- Cabral, A. M., Trabelsi, W., Serra, R., Montemor, M. F., Zheludkevich, M. L., and Ferreira, M. G. S. (2006). The corrosion resistance of hot dip galvanized steel and AA2024-T3 pre-treated with bis-[triethoxysilylpropyl] tetraulfide solutions doped with Ce(NO₃)₃. *Corros. Sci.* 48, 3740–3758. doi: 10.1016/j.corsci.2006.01.010
- Cole, K. S., and Cole, R. H. (1942). Dispersion and absorption in dielectrics II. Direct current characteristics. *J. Chem. Phys.* 10, 98–105. doi: 10.1063/1.1723677
- Colombani, O., Ruppel, M., Schubert, F., Zettl, H., Pergushov, D. V., and Müller, A. H. E. (2007). Synthesis of Poly(n-butyl acrylate)-block-poly(acrylic acid) diblock copolymers by ATRP and their micellization in water. *Macromolecules* 40, 4338–4350. doi: 10.1021/ma0609578
- Comstock, M. J., Hertzberg, R. W., and Riew, C. K. (1989). Rubber-toughened plastics, copyright, advances in chemistry series, FOREWORD, ABOUT THE EDITOR, Dedication. *Adv. Chem.* 222, i–x. doi: 10.1021/ba-1989-0222.fw001
- Das, R., Melchior, C., and Karumbaiah, K. M. (2016). Chapter 11: Self-healing composites for aerospace applications. *Adv. Compos. Mater. Aerospace Eng.* 333–364. doi: 10.1016/b978-0-08-100037-3.00011-0
- de Damborenea, J., Conde, A., and Arenas, M. A. (2014). "3 - Corrosion inhibition with rare earth metal compounds in aqueous solutions," in *Rare Earth-Based Corrosion Inhibitors*, eds M. Forsyth and B. Hinton (Cambridge, UK: Woodhead Publishing), 84–116.
- D'Hollander, S., Van Assche, G., Van Mele, B., and Du Prez, F. (2009). Novel synthetic strategy toward shape memory polyurethanes with a well-defined switching temperature. *Polymer* 50, 4447–4454. doi: 10.1016/j.polymer.2009.07.021
- Figueira, R. B., Silva, C. J. R., and Pereira, E. V. (2014). Organic–inorganic hybrid sol–gel coatings for metal corrosion protection: a review of recent progress. *J. Coat. Technol. Res.* 12, 1–35. doi: 10.1007/s11998-014-9595-6
- Foyet, A., Wu, T. H., Kodentsov, A., van der Ven, L. G. J., de With, G., and van Benthem, R. A. T. M. (2013). Corrosion protection and delamination mechanism of epoxy/carbon black nanocomposite coating on AA2024-T3. *J. Electrochem. Soc.* 160, C159–C167. doi: 10.1149/2.086304jes
- Garg, A., and Mai, Y. W. (1988). Failure mechanisms in toughened epoxy resins—A review. *Compos. Sci. Technol.* 31, 179–223. doi: 10.1016/0266-3538(88)90009-7
- Gharbi, O., Thomas, S., Smith, C., and Birbilis, N. (2018). Chromate replacement: what does the future hold? *npj Mater. Degrad.* 2, 1–2. doi: 10.1038/s41529-018-0034-5
- Hinton, B. R. W. (1992). Corrosion inhibition with rare earth metal salts. *J. Alloys Compd.* 180, 15–25. doi: 10.1016/0925-8388(92)90359-H
- Hinton, B. R. W., and Wilson, L. (1989). The corrosion inhibition of zinc with cerous chloride. *Corros. Sci.* 29, 967–985. doi: 10.1016/0010-938X(89)90087-5
- Hsu, C. H., and Mansfeld, F. (2001). Technical note: concerning the conversion of the constant phase element parameter Y₀ into a capacitance. *Corrosion* 57, 747–748. doi: 10.5006/1.3280607
- Hughes, A. E., Harvey, T. G., Birbilis, N., Kumar, A., and Buchheit, R. G. (2014). "7 - Coatings for corrosion prevention based on rare earths," in *Rare Earth-Based Corrosion Inhibitors*, eds M. Forsyth and B. Hinton (Cambridge, UK: Woodhead Publishing), 186–232.
- Iijima, T., Horiba, T., and Tomoi, M. (1991). Toughening of epoxy resins by modification with reactive elastomers composed of butyl acrylate, glycidyl methacrylate and acrylonitrile or styrene. *Eur. Polym. J.* 27, 1231–1238. doi: 10.1016/0014-3057(91)90060-2
- Jorcin, J.-B., Scheltjens, G., Van Ingelgem, Y., Tourwé, E., Van Assche, G., De Graeve, I., et al. (2010). Investigation of the self-healing properties of shape memory polyurethane coatings with the 'odd random phase multisine' electrochemical impedance spectroscopy. *Electrochim. Acta* 55, 6195–6203. doi: 10.1016/j.electacta.2010.01.027
- Kainourgios, P., Kartsonakis, I. A., Dragatogiannis, D. A., Koumoulos, E. P., Goulis, P., and Charitidis, C. A. (2017). Electrochemical surface functionalization of carbon fibers for chemical affinity improvement with epoxy resins. *Appl. Surf. Sci.* 416, 593–604. doi: 10.1016/j.apsusc.2017.04.214
- Kakaroglou, A., Domini, M., and De Graeve, I. (2016). Encapsulation and incorporation of sodium molybdate in polyurethane coatings and study of its corrosion inhibition on mild steel. *Surf. Coat. Technol.* 303, 330–341. doi: 10.1016/j.surfcoat.2016.02.007
- Kartsonakis, I. A., Balaskas, A. C., Koumoulos, E. P., Charitidis, C. A., and Kordas, G. (2013). ORMOSIL-epoxy coatings with ceramic containers for corrosion protection of magnesium alloys ZK10. *Prog. Organic Coat.* 76, 459–470. doi: 10.1016/j.porgcoat.2012.10.028
- Kartsonakis, I. A., Balaskas, A. C., Koumoulos, E. P., Charitidis, C. A., and Kordas, G. C. (2012). Incorporation of ceramic nanocontainers into epoxy coatings for the corrosion protection of hot dip galvanized steel. *Corros. Sci.* 57, 30–41. doi: 10.1016/j.corsci.2011.12.037
- Kartsonakis, I. A., Danilidis, I. L., Pappas, G. S., and Kordas, G. C. (2010). Encapsulation and release of corrosion inhibitors into titania nanocontainers. *J. Nanosci. Nanotechnol.* 10, 5912–5920. doi: 10.1166/jnn.2010.2571
- Kartsonakis, I. A., Liatsi, P., Daniilidis, I., and Kordas, G. (2008). Synthesis, characterization, and antibacterial action of hollow ceria nanospheres with/without a conductive polymer coating. *J. Am. Ceramic Soc.* 91, 372–378. doi: 10.1111/j.1551-2916.2007.02088.x
- Kartsonakis, I. A., Stanciu, S. G., Matei, A. A., Hristu, R., Karantonis, A., and Charitidis, C. A. (2016). A comparative study of corrosion inhibitors on hot-dip galvanized steel. *Corros. Sci.* 112, 289–307. doi: 10.1016/j.corsci.2016.07.030
- Kawasaki, A., Furukawa, J., Tsuruta, T., Wasai, G., and Makimoto, T. (1961). Infrared Spectra of Poly(butyl acrylates). *Die Makromolekulare Chemie* 49, 76–111. doi: 10.1002/macp.1961.020490108
- Kongparakul, S., Kornprasert, S., Suriya, P., Le, D., Samart, C., Chantarasiri, N., et al. (2017). Self-healing hybrid nanocomposite anticorrosive coating from epoxy/modified nanosilica/perfluorooctyl triethoxysilane. *Prog. Org. Coat.* 104, 173–179. doi: 10.1016/j.porgcoat.2016.12.020
- Levina, A., Harris, H. H., and Lay, P. A. (2006). Binding of chromium(VI) to histones: implications for chromium(VI)-induced genotoxicity. *J. Biol. Inorg. Chem.* 11, 225–234. doi: 10.1007/s00775-005-0068-3
- Li, G. L., Hu, J., Wang, H., Pilz-Allen, C., Wang, J., Qi, T., et al. (2017). Polymer-decorated anisotropic silica nanotubes with combined shape and surface properties for guest delivery. *Polymer* 109, 332–338. doi: 10.1016/j.polymer.2016.12.048
- Li, H., Wang, W., Tan, J., Li, C., and Zhang, Q. (2015). Synthesis and characterization of graft copolymers PnBA-g-PS by miniemulsion polymerization. *RSC Adv.* 5, 45459–45466. doi: 10.1039/C5RA06502J

- Li, Q., Wu, G., Zhang, X., and Wu, C. (2006). Preparation of Poly (n-butyl acrylates) encapsulated carbon black via ultrasonic irradiation initiating emulsion polymerization. *Polym. J.* 38, 1245–1250. doi: 10.1295/polymj.PJ2006053
- Luo, X., and Mather, P. T. (2013). Shape memory assisted self-healing coating. *ACS Macro Lett.* 2, 152–156. doi: 10.1021/mz400017x
- Lyon, S. B., Bingham, R., and Mills, D. J. (2017). Advances in corrosion protection by organic coatings: what we know and what we would like to know. *Prog. Org. Coat.* 102, 2–7. doi: 10.1016/j.porgcoat.2016.04.030
- McGarry, F. J. (1970). Building design with fibre reinforced materials. *Proc. R. Soc. A Math. Phys. Eng. Sci.* 319, 59–68. doi: 10.1098/rspa.1970.0165
- Meng, F., Liu, L., Tian, W., Wu, H., Li, Y., Zhang, T., et al. (2015). The influence of the chemically bonded interface between fillers and binder on the failure behaviour of an epoxy coating under marine alternating hydrostatic pressure. *Corros. Sci.* 101, 139–154. doi: 10.1016/j.corsci.2015.09.011
- Moharram, M. A., and Khafagi, M. G. (2007). Application of FTIR spectroscopy for structural characterization of ternary poly(acrylic acid)–metal–poly(vinyl pyrrolidone) complexes. *J. Appl. Polym. Sci.* 105, 1888–1893. doi: 10.1002/app.25703
- Moharram, M. A., Rabie, S. M., and El-Gendy, H. M. (2002). Infrared spectra of γ -irradiated poly(acrylic acid)–polyacrylamide complex. *J. Appl. Polym. Sci.* 85, 1619–1623. doi: 10.1002/app.10702
- Montemor, M. F., Trabelsi, W., Lamaka, S. V., Yasakau, K. A., Zheludkevich, M. L., Bastos, A. C., et al. (2008). The synergistic combination of bisilane and CeO₂-ZrO₂ nanoparticles on the electrochemical behaviour of galvanised steel in NaCl solutions. *Electrochim. Acta* 53, 5913–5922. doi: 10.1016/j.electacta.2008.03.069
- Njoku, D. I., Cui, M., Xiao, H., Shang, B., and Li, Y. (2017). Understanding the anticorrosive protective mechanisms of modified epoxy coatings with improved barrier, active and self-healing functionalities: EIS and spectroscopic techniques. *Sci. Rep.* 7:15597. doi: 10.1038/s41598-017-15845-0
- O’Keefe, M. J., Fahrenholtz, W. G., Stoffer, J. O., and Morris, E. L. (2014). “6 - Corrosion-resistant polymer coatings containing rare earth compounds,” in *Rare Earth-Based Corrosion Inhibitors*, eds M. Forsyth and B. Hinton (Cambridge, UK: Woodhead Publishing), 163–185.
- Orazem, M. E., and Tribollet, B. (eds.). (2008). “Time-constant dispersion 13.1 constant phase elements,” in *Electrochemical Impedance Spectroscopy* (Hoboken, NJ: Wiley), 233–237.
- OSHA3373-10 (2009). *Hexavalent Chromium*. Hoboken, NJ: Occupational Safety and Health Administration; U.S. Department of Labor.
- Parameswaranpillai, J., Hameed, N., Pionteck, J., and Woo, E. M. (2017). *Handbook of Epoxy Blends*. Cham: Springer International Publishing.
- Plawecka, M., Snihirova, D., Martins, B., Szczepanowicz, K., Warszynski, P., and Montemor, M. F. (2014). Self healing ability of inhibitor-containing nanocapsules loaded in epoxy coatings applied on aluminium 5083 and galvanized substrates. *Electrochim. Acta* 140, 282–293. doi: 10.1016/j.electacta.2014.04.035
- Pourbaix, M., and de Zoubov, N. (1966). *Atlas of Electrochemical Equilibria in Aqueous Solutions*. New York, NY: Pergamon Press, 307.
- Qiao, Y., Li, W., Wang, G., Zhang, X., and Cao, N. (2015). Application of ordered mesoporous silica nanocontainers in an anticorrosive epoxy coating on a magnesium alloy surface. *RSC Adv.* 5, 47778–47787. doi: 10.1039/c5ra05266a
- Ratna, D. (2001). Phase separation in liquid rubber modified epoxy mixture. Relationship between curing conditions, morphology and ultimate behavior. *Polymer* 42, 4209–4218. doi: 10.1016/s0032-3861(00)00798-9
- Ratna, D., and Banthia, A. K. (2004). Rubber toughened epoxy. *Macromol. Res.* 12, 11–21. doi: 10.1007/bf03218989
- Samiee, R., Ramezanzadeh, B., Mahdavian, M., and Alibakhshi, E. (2019). Assessment of the smart self-healing corrosion protection properties of a water-base hybrid organo-silane film combined with non-toxic organic/inorganic environmentally friendly corrosion inhibitors on mild steel. *J. Clean. Prod.* 220, 340–356. doi: 10.1016/j.jclepro.2019.02.149
- Sierra-Ávila, R., Pérez-Alvarez, M., Cadenas-Pliego, G., Comparán Padilla, V., Ávila-Orta, C., Pérez Camacho, O., et al. (2015). Synthesis of copper nanoparticles using mixture of allylamine and polyallylamine. *J. Nanomater.* 2015, 1–9. doi: 10.1155/2015/367341
- Skorb, E. V., Fix, D., Andreeva, D. V., Möhwald, H., and Shchukin, D. G. (2009). Surface-modified mesoporous SiO₂ containers for corrosion protection. *Adv. Funct. Mater.* 19, 2373–2379. doi: 10.1002/adfm.200801804
- Snihirova, D., Lamaka, S. V., and Montemor, M. F. (2016). Part II: Smart composite coatings for corrosion protection of aluminium alloys in aerospace applications. *Smart Compos. Coat. Membr.* Part II, 85–121. doi: 10.1016/b978-1-78242-283-9.00004-x
- Soares, B. G., and Livi, S. (2017). “Novel techniques for the preparation of different epoxy/rubber blends,” in *Handbook of Epoxy Blends*, eds J. Parameswaranpillai, N. Hameed, J. Pionteck and E. M. Woo (Cham: Springer International Publishing), 29–67.
- Souza, J. P. B., and Reis, J. M. L. (2013). Thermal behavior of DGEBA (Diglycidyl Ether of Bisphenol A) adhesives and its influence on the strength of joints. *Appl. Adhes. Sci.* 1:6. doi: 10.1186/2196-4351-1-6
- Tania, R., Ciontea, L., Suci, R.-C., Petrisor, T. Jr., Gabor, M., Thalmayer, G., et al. (2008). Thermal decomposition study by DTA-TG-MS of cerium[III] acetylacetonate used as ceria thin film precursor. *J. Optoelectron. Adv. Mater.* 10, 2223–2227. Available online at: <https://www.tib.eu/en/search/id/BLSE%3ARN237661951/Thermal-decomposition-study-by-DTA-TG-MS-of-cerium/>
- Thierry, D., Massinon, D., and Hugot-Le-Goff, A. (1991). *In situ* determination of corrosion products formed on painted galvanized steel by raman spectroscopy. *J. Electrochem. Soc.* 138, 879–880. doi: 10.1149/1.2085702
- Trabelsi, W., Triki, E., Dhoubi, L., Ferreira, M. G. S., Zheludkevich, M. L., and Montemor, M. F. (2006). The use of pre-treatments based on doped silane solutions for improved corrosion resistance of galvanized steel substrates. *Surf. Coat. Technol.* 200, 4240–4250. doi: 10.1016/j.surfcoat.2005.01.044
- Ubaid, F., Radwan, A. B., Naeem, N., Shakoob, R. A., Ahmed, Z., Montemor, M. F., et al. (2019). Multifunctional self-healing polymeric nanocomposite coatings for corrosion inhibition of steel. *Surf. Coat. Technol.* 372, 121–133. doi: 10.1016/j.surfcoat.2019.05.017.
- Uhlig, H. R. (2008). *Corrosion and Corrosion Control: An Introduction to Corrosion Science and Engineering*, ed W. Revie Hoboken, NJ: John Wiley and Sons, Inc.
- Ulaeto, S. B., Rajan, R., Pancrecius, J. K., Rajan, T. P. D., and Pai, B. C. (2017). Developments in smart anticorrosive coatings with multifunctional characteristics. *Prog. Org. Coat.* 111, 294–314. doi: 10.1016/j.porgcoat.2017.06.013
- Unnikrishnan, K. P., and Thachil, E. T. (2012). Toughening of epoxy resins. *Design. Monom. Polym.* 9, 129–152. doi: 10.1163/15685506776382664
- Upadhyay, V., and Battocchi, D. (2016). Localized electrochemical characterization of organic coatings: a brief review. *Prog. Org. Coat.* 99, 365–377. doi: 10.1016/j.porgcoat.2016.06.012
- Vázquez, A., Rojas, A. J., Adabbo, H. E., Borrajo, J., and Williams, R. J. J. (1987). Rubber-modified thermosets: Prediction of the particle size distribution of dispersed domains. *Polymer* 28, 1156–1164. doi: 10.1016/0032-3861(87)90259-x
- Verchere, D., Sautereau, H., Pascault, J. P., Moschiar, S. M., Riccardi, C. C., and Williams, R. J. J. (1990). Rubber-modified epoxies. I. Influence of carboxyl-terminated butadiene-acrylonitrile random copolymers (CTBN) on the polymerization and phase separation processes. *J. Appl. Polym. Sci.* 41, 467–485. doi: 10.1002/app.1990.070410303
- Williams, R. J. J., Rozenberg, B. A., and Pascault, J.-P. (1997). “Reaction-induced phase separation in modified thermosetting polymers,” in *Polymer Analysis Polymer Physics*. Berlin; Heidelberg: Springer, 95–156. Available online at: <https://link.springer.com/content/pdf/bfm%3A978-3-540-68374-2%2F1.pdf>
- Yamanaka, K., Takagi, Y., and Inoue, T. (1989). Reaction-induced phase separation in rubber-modified epoxy resins. *Polymer* 30, 1839–1844. doi: 10.1016/0032-3861(89)90355-8
- Yao, Z., Braid, N., Botton, G. A., and Adronov, A. (2003). Polymerization from the surface of single-walled carbon nanotubes - preparation and characterization of nanocomposites. *J. Am. Chem. Soc.* 125, 16015–16024. doi: 10.1021/ja037564y
- Yasakau, K. A., Ferreira, M. G. S., Zheludkevich, M. L., Terryn, H., Mol, J. M. C., and Gonzalez-Garcia, Y. (2014). “8 - Novel and self-healing anticorrosion coatings using rare earth compounds,” in *Rare Earth-Based Corrosion Inhibitors*, eds M. Forsyth and B. Hinton (Cambridge, UK: Woodhead Publishing), 233–266.

- Yee, A. F., and Pearson, R. A. (1986). Toughening mechanisms in elastomer-modified epoxies. *J. Mater. Sci.* 21, 2462–2474. doi: 10.1007/bf01114293
- Yin, X., Liu, Z., Wang, D., Pei, X., Yu, B., and Zhou, F. (2015). Bioinspired self-healing organic materials: chemical mechanisms and fabrications. *J. Bionic Eng.* 12, 1–16. doi: 10.1016/s1672-6529(14)60095-0
- Zhang, F., Ju, P., Pan, M., Zhang, D., Huang, Y., Li, G., et al. (2018). Self-healing mechanisms in smart protective coatings: a review. *Corros. Sci.* 144, 74–88. doi: 10.1016/j.corsci.2018.08.005
- Zhang, J.-T., Hu, J.-M., Zhang, J.-Q., and Cao, C.-N. (2004). Studies of water transport behavior and impedance models of epoxy-coated metals in NaCl solution by EIS. *Prog. Org. Coat.* 51, 145–151. doi: 10.1016/j.porgcoat.2004.08.001
- Zheludkevich, M. (2009). “Self-healing anticorrosion coatings,” in *Self-Healing Materials*, ed S. K. Ghosh (Weinheim: WILEY-VCH Verlag GmbH & Co. KGaA), 101–139.
- Zheludkevich, M. L., Serra, R., Montemor, M. F., Yasakau, K. A., Salvado, I. M. M., and Ferreira, M. G. S. (2005). Nanostructured sol-gel coatings doped with cerium nitrate as pre-treatments for AA2024-T3. *Electrochim. Acta* 51, 208–217. doi: 10.1016/j.electacta.2005.04.021
- Zhu, D. Y., Rong, M. Z., and Zhang, M. Q. (2015). Self-healing polymeric materials based on microencapsulated healing agents: from design to preparation. *Prog. Polym. Sci.* 49–50, 175–220. doi: 10.1016/j.progpolymsci.2015.07.002
- Zhu, Y., Free, M. L., and Yi, G. (2016). The effects of surfactant concentration, adsorption, aggregation, and solution conditions on steel corrosion inhibition and associated modeling in aqueous media. *Corros. Sci.* 102, 233–250. doi: 10.1016/j.corsci.2015.10.012

Conflict of Interest Statement: The authors declare that the research was conducted in the absence of any commercial or financial relationships that could be construed as a potential conflict of interest.

Copyright © 2019 Karaxi, Kartsonakis and Charitidis. This is an open-access article distributed under the terms of the Creative Commons Attribution License (CC BY). The use, distribution or reproduction in other forums is permitted, provided the original author(s) and the copyright owner(s) are credited and that the original publication in this journal is cited, in accordance with accepted academic practice. No use, distribution or reproduction is permitted which does not comply with these terms.